ACS APPLIED MATERIALS & INTERFACES

www.acsami.org

Research Article

Corrosion Resistance and Cytocompatibility of Magnesium–Calcium Alloys Modified with Zinc- or Gallium-Doped Calcium Phosphate Coatings

Dilara Goksu Tamay, Seyda Gokyer, Jürgen Schmidt, Alina Vladescu,*,†† Pinar Yilgor Huri, Vasif Hasirci, and Nesrin Hasirci*,††

Cite This: *ACS Appl. Mater. Interfaces* 2022, 14, 104–122

Read Online

ACCESS | Metrics & More | Article Recommendations | Supporting Information

ABSTRACT: In orthopedic surgery, metals are preferred to support or treat damaged bones due to their high mechanical strength. However, the necessity for a second surgery for implant removal after healing creates problems. Therefore, biodegradable metals, especially magnesium (Mg), gained importance, although their extreme susceptibility to galvanic corrosion limits their applications. The focus of this study was to control the corrosion of Mg and enhance its biocompatibility. For this purpose, surfaces of magnesium–calcium (MgCa1) alloys were modified with calcium phosphate (CaP) or CaP doped with zinc (Zn) or gallium (Ga) via microarc oxidation. The effects of surface modifications on physical, chemical, and mechanical properties and corrosion resistance of the alloys were studied using surface profilometry, goniometry, scanning electron microscopy (SEM), energy-dispersive X-ray spectroscopy (EDS), nanoindentation, and electrochemical impedance spectroscopy (EIS). The coating thickness was about 5–8 μm, with grain sizes of 43.1 nm for CaP coating and 28.2 and 58.1 nm for Zn- and Ga-doped coatings, respectively. According to EIS measurements, the capacitive response (Y_c) decreased from 11.29 to 8.72 and 0.15 Ω^{-1} cm^{-2} s^n upon doping with Zn and Ga, respectively. The E_{corr} value, which was −1933 mV for CaP-coated samples, was found significantly electropositive at −275 mV for Ga-doped ones. All samples were cytocompatible according to indirect tests. *In vitro* culture with Saos-2 cells led to changes in the surface compositions of the alloys. The numbers of cells attached to the Zn-doped (2.6×10^4 cells/cm^2) and Ga-doped (6.3×10^4 cells/cm^2) coatings were higher than that on the surface of the undoped coating (1.0×10^3 cells/cm^2). Decreased corrosivity and enhanced cell affinity of the modified MgCa alloys (CaP coated and Zn and Ga doped, with Ga-doped ones having the greatest positive effect) make them novel and promising candidates as biodegradable metallic implant materials for the treatment of bone damages and other orthopedic applications.

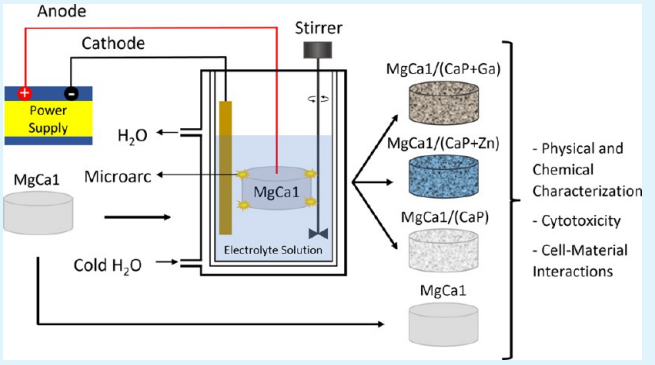

KEYWORDS: *biodegradable magnesium implants, microarc oxidation, calcium phosphate coating, zinc, gallium*

1. BACKGROUND

Metals have been used in the repair of damaged and/or nonfunctioning organs and tissues for many years.[1] Although some novel materials such as polymers, ceramics, and their composites are replacing metals in many applications, use of metallic implants is still preferred in orthopedic applications due to their exceptional mechanical strength, especially in the treatment of defects in load-bearing bones.[2−4] To eliminate the need for a second surgery for the removal of metallic implants after completion of the healing process, or due to outgrowth of the implant in pediatric cases, researchers focused on biodegradable metals. These materials gradually degrade within the body upon implantation but maintain their strength at a satisfactory level until the tissue regeneration process is complete. An important consideration for these metals is that their degradation products should be tolerable by the body.[5] Magnesium (Mg)-based alloys are the most commonly studied biodegradable metals in this regard.[6−8] Mg has the advantages of being lightweight with a density of 1.74−2.0 g/cm^3, a value that is close to the density of the natural bone and much less than that of titanium or stainless steel (ca. 4.5 and 7.8 g/cm^3, respectively).[9,10] In addition, Mg is an essential element required in a broad variety of physiological functions.[11]

Received: August 25, 2021
Accepted: December 14, 2021
Published: December 27, 2021

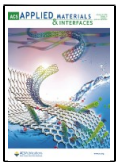

Table 1. Electrolyte Composition and the Microarc Oxidation (MAO) Parameters

samples	electrolyte components (g/L for solids and mL/L for liquids)		pH	conductivity (mS/cm)	applied voltage (V)
MgCa1 (uncoated control)					
MgCa1/(CaP) (calcium phosphate coating)	potassium dihydrogen phosphate [KH_2PO_4]	15	10.2	43.8	275
	ethylenediamine [$C_2H_8N_2$]	60			
	ammonia water [NH_4OH] (25%)	50			
	ammonium dihydrogen phosphate [$NH_4H_2PO_4$]	17			
	sodium calcium edetate [$C_{10}H_{12}N_2O_8CaNa_2$]	35			
MgCa1/(CaP+Zn) (CaP coating doped with zinc)	potassium dihydrogen phosphate [KH_2PO_4]	45	11.3	33.6	250
	ethylenediamine [$C_2H_8N_2$]	60			
	ammonia water [NH_4OH] (25%)	50			
	ammonium dihydrogen phosphate [$NH_4H_2PO_4$]	17			
	sodium calcium edetate [$C_{10}H_{12}N_2O_8CaNa_2$]	45			
	zinc nitrate [$Zn(NO_3)_2$]	30			
MgCa1/(CaP+Ga) (CaP coating doped with gallium)	potassium dihydrogen phosphate [KH_2PO_4]	25	10.7	33.2	295
	ethylenediamine [$C_2H_8N_2$]	60			
	ammonia water [NH_4OH] (25%)	50			
	ammonium dihydrogen phosphate [$NH_4H_2PO_4$]	17			
	sodium calcium edetate [$C_{10}H_{12}N_2O_8CaNa_2$]	35			
	gallium nitrate [$Ga(NO_3)_3$]	8.8			

One drawback of pure Mg is its high corrosion rate, which is accompanied by the rapid release of ions and hydrogen gas in the physiological medium.[12,13] Furthermore, when there are traces of iron, nickel, or copper in the metal, the degradation rate increases significantly.[14] To control the rapid hydrogen gas release, alloying Mg with other elements such as aluminum (Al), calcium (Ca), strontium (Sr), manganese (Mn), zirconium (Zr), tin (Sn), zinc (Zn), rare-earth elements, and ytterbium (Yb) was studied.[15,16] Another issue with pure Mg is that its mechanical strength is not high enough for use in load-bearing applications. The tensile strength for cast Mg metal is reported as 21 MPa, which increases to approximately 100 MPa for extruded and 140 MPa for rolled metal,[17] while the tensile strength of the femur is reported as 92−188 MPa.[18] These also point out to the need for new Mg alloys with enhanced mechanical properties.[19,20]

New alloys of Mg could be prepared for use in medical applications by modifying their microstructure,[7] mechanical strength,[21] osteogenic properties,[22,23] degradation rates,[18] and degradation products.[24−26] It has been shown that coating the surface of magnesium alloys with various metals or modification of the surface structure by creating nanodesigns, pores, or crystals enhances the biocompatibility of Mg alloys.[27−31] Alloying Mg with Ca improves the osteoconductive bioactivity of Mg as well as its thermal stability, but this may increase the corrosion rate.[32] In physiological media, a Mg-based biodegradable metal implant is oxidized by producing metal ions and electrons. The electrons cause reduction of water, forming hydrogen gas (H_2) and hydroxide ions (OH^-). These OH^- ions can further react with the metal, forming metal hydroxide (MOH) layers on the surface, which can decrease the rate of dissolution.[7] Meanwhile, some macromolecules such as proteins or lipids may adsorb on the surface, delay the degradation, and enhance cell attachment and bond integrity.[33,34] Upon protein adsorption, cell affinity toward the surface of the metal also increases; more cells attach to the surface start proliferating and depositing extracellular matrix (ECM) to regenerate the tissue. All of these reactions change the physiological equilibrium in the microenvironment of the implant.[35,36]

Hydrogen gas formed during the corrosion may act as an antioxidant; it has preventative and therapeutic effects on many acute oxidative stress-induced diseases, including neonatal cerebral hypoxia, Parkinson's disease, ischemia, or reperfusion of the spinal cord, heart, lung, liver, kidney, and intestine.[37,38] On the other hand, subcutaneous emphysema caused by H_2 gas may cause discomfort in patients, and lead to further complications such as toxicity due to alkalization of the local environment, tissue necrosis as a result of surgical wound reopening, and defects in the regenerating bone tissue.[39,40] To overcome this problem, calcium phosphate (CaP) coatings are often applied to the surface of Mg-based orthopedic implants using various methods.[41] Alloying with Ca allows tailoring of the degradation behavior of Mg-based implants for specific *in vivo* applications, as the degradation rate changes with the Ca content of the alloy.[42,43] Introduction of other elements to Mg−Ca binary alloys also improves the *in vivo* performance of the material. For example, improved mechanical strength and degradation properties were reported for Zn-added Mg−Ca binary alloys,[44] while Ga addition enhanced corrosion resistance, bone-implant bonding, and osteoblast regeneration.[41,45] Bazhenov and colleagues investigated the mechanical strength and corrosion properties of a Mg−Ga−Zn system and the alloy with a 4% (w/w) Zn and Ga content was proposed as a suitable implant material.[46]

The aim of this study was to develop surface-modified Mg−Ca binary alloy-based biodegradable metallic implant materials with a controlled corrosion rate and enhanced biocompatibility. For this purpose, MgCa alloys (denoted MgCa1) were prepared, and their surfaces were modified with calcium phosphate (CaP) coatings containing Zn or Ga by a microarc oxidation process. The Zn element was selected as a dopant due to its stimulatory effect on osteoblast growth[47,48] and prominent antibacterial and antifungal effects.[49−52] Ga was selected as a dopant as it was shown to improve biological fixation[45,53] and exhibit low in vitro

https://doi.org/10.1021/acsami.1c16307
ACS Appl. Mater. Interfaces 2022, 14, 104−122

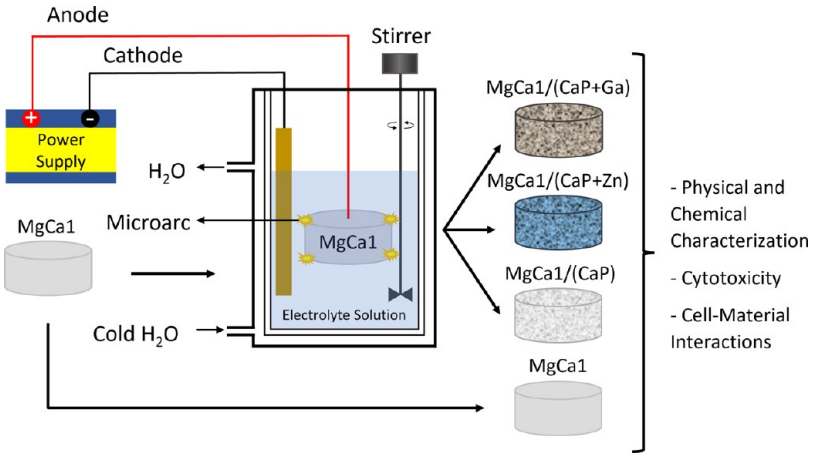

Figure 1. Schematic presentation of preparation of alloys and the tests carried out.

cytotoxicity.[54] Physical, chemical, and structural properties of the alloys were studied with surface profilometry, goniometry, X-ray diffractometry (XRD), scanning electron microscopy (SEM), and energy-dispersive X-ray spectroscopy (EDS). Moreover, the mechanical properties of the coatings applied to MgCa1 alloy were investigated in terms of hardness, adhesion, roughness, and elastic modulus. *In vitro* corrosion resistance was evaluated by electrochemical tests to determine the efficacy of the coatings against corrosive attacks. Indirect cytotoxicity tests were conducted with fibroblast cell line L929, and material−cell interactions were investigated by culturing with the human bone cancer (osteosarcoma) cell line, Saos-2. Changes in physical, chemical, and structural properties of the alloys upon cell culture were also investigated with the aforementioned characterization techniques.

2. MATERIALS AND METHODS

2.1. Materials. Magnesium−calcium binary alloy was obtained from Helmholtz Centre Geesthacht (Germany). Potassium dihydrogen phosphate [KH_2PO_4] was purchased from Carl Roth GmbH + Co. (Germany). Ammonium dihydrogen phosphate [$NH_4H_2PO_4$] was purchased from VWR Chemicals. Ethylenediamine [$C_2H_8N_2$], zinc nitrate [$Zn(NO_3)_2$], and sodium calcium edetate [$C_{10}H_{12}N_2O_8CaNa_2$] were obtained from Sigma-Aldrich (Germany). Gallium nitrate [$Ga(NO_3)_3$] was purchased from Alfa Aesar. RPMI 1640 (w/ 2 mM L-glutamine), fetal bovine serum (FBS, heat inactivated, EU grade), trypsin−EDTA solution B (0.25% trypsin, 0.05% EDTA), and penicillin/streptomycin (100 U·mL^{-1}/100 μg·mL^{-1}) were obtained from Biological Industries (Israel). The live−dead cell viability/cytotoxicity kit (for mammalian cells) was purchased from Thermo Fisher. Dulbecco's modified Eagle's medium (DMEM) (w/ 3.7 g/L $NaHCO_3$ and 4.5 g/L D-glucose, w/o L-glutamine and phenol red), DMEM high-glucose powder, and ammonia water [NH_4OH] (25%) were purchased from Merck (Germany). L-Glutamine (200 mM) was a product of Lonza (Switzerland).

2.2. Methods. *2.2.1. Preparation of Magnesium Alloys.* The magnesium−calcium alloy (MgCa1) containing 1.04% (w/w) Ca and less than 0.04% (w/w) Si, Al, Fe, Cu, Mn, Zn, or Zr was produced by the permanent mold direct chill casting technique. The cast ingots were cylindrical with 60 mm diameter and 170 mm length. These ingots were extruded to form rods that are 15 mm in diameter and then divided into 3 mm thick disk-shaped samples by means of mechanical processing (CNC turning). These disk-shaped MgCa1 samples were then surface modified by the microarc oxidation technique using different aqueous electrolyte solutions, where the composition of the electrolytes determined the composition of the coating layers obtained. The samples prepared, electrolyte compositions, and the microarc oxidation (MAO) parameters used in the study are given in Table 1. All samples were used in *in vitro* cytotoxicity and cell−material interaction experiments, as well as in characterization tests before and after cell culture. The experimental scheme is presented in Figure 1.

2.2.2. Physical, Chemical, and Mechanical Characterizations. 2.2.2.1. Thickness, Phase Composition, and Ca/P Ratio of the Coatings. Coating thicknesses were determined with a reversed incident light microscope (DMi8, Leica, Germany). The samples were metallographically prepared to measure the coating thickness. Briefly, the samples were embedded in epoxy resin and ground flat with 500 grit silicon−carbide sandpaper (SAPHIR 250, ATM Qness GmbH, Germany) and then with 1200 grit silicon−carbide sandpaper for 1 min. After grinding, samples were cleaned ultrasonically in distilled water for 1 min and polished with diamond paste (from 9 to 1 μm grit) for 5 min, cleaning with alcohol after each change of the grit size. The final polishing was achieved with a special alcohol-based polish Etosil E (ATM Qness GmbH, Germany) for 1 min. Afterward, the polish was cleaned again with alcohol and dried with hot air.

The phase composition was evaluated by the grazing-incidence X-ray diffraction (XRD) technique using a SmartLab diffractometer with Cu Kα radiation (Rigaku) from 20 to 100° with a step size of 0.02°/min and an incident angle of 3°. The analyses were performed in accordance with ISO 13779-3:2018.

The Ca/P ratio was determined by the energy-dispersive spectrometry (EDS) module (Bruker, Germany) of a scanning electron microscope (SEM, TM3030 Plus, Hitachi, Japan).

2.2.2.2. In Vitro Corrosion Resistance. Electrochemical tests were performed using a potentiostat/galvanostat (VersaSTAT 3, Princeton Applied Research), and the data were recorded using VersaStudio (Princeton Applied Research) software, according to the ASTM G5-94 standard (reapproved 2011). The tests were performed in DMEM solution at 37 ± 0.5 °C. For this purpose, a classical three-electrode cell was used with platinum as the counter electrode, a saturated calomel electrode (SCE) as the reference electrode, and the investigated samples as the working electrode (with 1 cm^2 exposed area, mounted in a Teflon holder). Prior to testing, the samples were monitored for 1 h while the open-circuit potential (E_{oc}) in time was recorded. A magnetic stirrer was used at a low agitation rate to disperse and eliminate frequently formed gas bubbles resulting from the reactivity of magnesium samples with the DMEM solution.

Electrochemical impedance spectroscopy (EIS) was also performed to investigate the electrochemical behavior of the materials, highlighting the properties of the coatings. The applied amplitude of the perturbation signal was 10 mV for root mean square versus E_{oc} in a frequency range of 0.2−10^4 Hz. The impedance data was displayed as Nyquist and Bode plots. Analysis of the spectra was performed by equivalent circuit fitting using Zview (Zview Inc., USA) software. The average error of the regression (χ^2) was used to describe the quality of the fit. Moreover, Tafel plots were obtained by applying a potential of −250 to 250 mV versus E_{oc}, with a scanning rate of 0.167 mV/s. EIS

https://doi.org/10.1021/acsami.1c16307
ACS Appl. Mater. Interfaces 2022, 14, 104−122

measurements were performed according to the ISO 16773-2:2016 standard.

2.2.2.3. Wettability and Surface Energy. Contact angles of all Mg-based alloys prepared were determined using a goniometer (Attension, Biolin Scientific, Sweden) by employing the sessile drop method. Water and *N*,*N*-dimethylformamide (DMF) drops (7 μL) were placed on the disk-shaped samples, and at least three drops were used to obtain statistically meaningful contact angle values for each liquid. Surface free energies (SFEs) were calculated from the measured contact angles using Zisman plots, where one minus cosine of the contact angle ($1-\cos\theta$) versus surface tension of the liquid (γ) was plotted.[55,56] The extrapolation of the line to the surface tension value that gives $\cos\theta = 1$ (the intercept at the *x*-axis) was noted as the surface free energy of the samples. The surface tension values for water and DMF at room temperature were taken as 72.04 mJ·m^{-2},[57] and 36.35 mJ·m^{-2},[58] respectively.

2.2.2.4. Mechanical Testing of the Coatings. **2.2.2.4.1 Hardness and Elastic Modulus**. The hardness of Mg-based implant materials was investigated using a nanoindentation system (Hysitron Premier TI, Bruker, Germany). For the tests, a Berkovich indenter with a radius of 100 nm and a total included angle of 142.30° was used. Prior to each test, a 15×15 μm^2 area was scanned at a normal force of 2 μN to study the roughness of the area where the indents will be performed. For each sample, at least three indents were carried out at 5 μm apart from each other using an applied force of 10 mN. The hardness and reduced modulus were determined using the Oliver−Pharr method. The tests were performed according to the protocol presented in ISO 14577-1:2002 standard (revised by ISO 14577-1:2015).[59,60]

2.2.2.4.2. Coat Adhesion. The adhesion of the coating to the alloy surface was evaluated by scratch tests using the UMT-TriboLab platform (Bruker, Germany) equipped with an acoustic sensor using the following parameters: indenter, 0.2 mm radius diamond tip; load, a continuous increase from 0 to 100 N; scratching speed, 10 mm/min; scratching distance, 10 mm (parameters were selected based on the EN1071-3:2005 standard). Failure of coat integrity was observed with an optical microscope, and the critical load (L_c), at which failure occurs, was determined using an acoustic sensor (EN1071-3/2005 standard).

2.2.3. Cytotoxicity, Cell Viability, and Cell−Substrate Interactions on Implant Materials. Material cytotoxicity and cell behavior on the Mg-based alloys were investigated by indirect cytotoxicity testing according to the ISO 10993-5 standard and direct cell−material interaction tests using the live−dead viability/cytotoxicity kit as described below. Samples were sterilized by immersion in 70% ethyl alcohol for 2 h prior to *in vitro* cell culture experiments.

2.2.3.1. Indirect Cytotoxicity. Indirect cytotoxicity tests were carried out using extracts of the alloys according to the ISO 10993/EN 30993 MEM-extraction test standard.[61] Briefly, the disk-shaped samples were sterilized by immersion in 70% ethyl alcohol solution for 2 h, washed with phosphate-buffered saline (PBS, pH 7.4, 10 mM), and then placed in falcon tubes containing 15 mL of DMEM high-glucose cell culture medium (supplemented with 10% FBS and 1% (v/v) penicillin (10 000 U/mL)/streptomycin (10 mg/mL)) at 37 °C for 24 h on a shaker incubator operating at 60 rpm to obtain extracts. Meanwhile, the L929 cell line was incubated in DMEM high-glucose culture media (supplemented with 10% FBS and 1% (v/v) penicillin (10 000 U/mL)/streptomycin (10 mg/mL)) for 24 h at standard culture conditions (37 °C, 5% CO_2). Cells were trypsinized and seeded in 12-well plates with a density of 10^4 cells/well. After 24 h of incubation, cells reached 70% confluency and the culture media was replaced with 1 mL of alloy extracts (syringe-filtered). Latex was used as a negative control, and ultrahigh-molecular-weight polyethylene (UHMWPE) was used as a positive control for all tests. After 72 h, cell viability was quantified using AlamarBlue reagent. Cytotoxicity of each implant extract on L929 cells was graded based on examinations of cell confluency, % dead cells present, morphological changes, and inhibition of cell growth under an inverted light microscope (Primovert, Zeiss, Germany) at 24, 48, and 72 h of incubation with the extracts. The results were compared with the ones obtained from negative and positive controls. All tests were conducted as triplets. A cytotoxicity index was obtained by adding the average of the scores obtained from the first three observations (confluency, dead cell percent, morphological change) to the score of the 4th observation (inhibition of cell growth). This index (which falls within a range of 0−8) was used to determine the cytotoxicity of the implant materials, with cytotoxicity index values between 0 and 3 indicating the material is not cytotoxic and 3−5 indicating the requirement of additional testing, and 5−8 indicating cytotoxicity.

2.2.3.2. Cell Viability. Cell viabilities on Mg-based alloys were assessed using the live−dead viability/cytotoxicity kit. For this purpose, human osteosarcoma cells (Saos-2) were incubated in a culture flask containing RPMI 1640 cell culture medium supplemented with 10% FBS and 1% penicillin/streptomycin in an incubator at 37 °C and 5% CO_2 until confluency, with cell medium refreshed every 2 days. Cells were lifted off the flask surface using trypsin−EDTA, centrifuged at 3000 rpm to collect the cell pellet, and resuspended in the complete culture medium. Saos-2 cells were seeded on each sample (sterilized by immersion in 70% ethanol for 2 h prior to experiments) with a cell density of 5×10^4 cells/sample and incubated in 24-well plates with complete culture medium at 37 °C and 5% CO_2 for 2 days. Cells with the same density were seeded in three empty wells as the tissue culture polystyrene (TCPS) control.

On day 2, cell viability was analyzed using the live−dead cell viability/cytotoxicity kit. Briefly, the culture medium was discarded, and samples and controls were washed with DMEM colorless medium supplemented with 1% penicillin/streptomycin. Samples and controls were then double-stained with Calcein-AM (2 μM, in 1 mL of DMEM colorless) and ethidium homodimer-1 (4 μM, in 1 mL of DMEM colorless) for 15 min at 37 °C and 5% CO_2 in an incubator. Cell viability on stained samples and controls was observed under a confocal laser scanning microscope (CLSM, LSM 800, Zeiss, Germany). Micrographs of different regions of interest (RoI) were analyzed using ImageJ (NIH) software to quantify cell viability.

2.2.3.3. Comparison of Surface Properties before and after Cell Culture. **2.2.3.3.1. Surface Roughness**. Surface roughness profiles of the Mg-based alloys with or without surface modifications were determined using a surface profilometer (S Neox, Sensofar, Spain) before and after 2 days of cell culture with osteosarcoma cell line Saos-2. Surface roughness profiles of the samples are given as the mean and standard deviation of the root mean square of heights (Sq) and arithmetical mean deviation of the assessed profile (Sa).

2.2.3.3.2 Surface Morphology and Chemistry. Surface morphologies of all samples before and after cell culture for 2 days were studied with a scanning electron microscope (QUANTA 400F Field Emission SEM, FEI, The Netherlands) after sputter coating with gold−palladium (Au-Pd) under an argon atmosphere. X-ray spectroscopy (EDS) (Bruker, Germany) was used to assess the chemical compositions of the surfaces. At least three random points were analyzed on each material surface, and atomic percentages (At %) obtained from each repetitive measurement were averaged. The statistically significant changes in the surface elemental composition before and after 2 days of cell culture for each group were analyzed with multiple *t*-tests. SEM and EDS analyses were also carried out for the samples after being kept in phosphate-buffered saline (PBS, pH 7.4, 10 mM) for one week after the cell culture tests.

2.2.4. Statistical Analysis. All in vitro tests were conducted with at least three biological repeats and three technical repeats where required. Data obtained from the measurements were evaluated comparatively using analysis of variance (ANOVA) and the Dunn−Sidak or Tukey test (multiple comparisons) with $\alpha = 0.05$ in GraphPad Prism 8.0.1 software (GraphPad Software Inc., La Jolla). Statistical analysis was performed before and after cell culture to compare the properties of the samples. Differences were noted not significant if *p*-values were more than 0.05 (ns: $p < 0.05$); significant if *p*-values were less than 0.05 (*: $p < 0.05$); and highly significant if *p*-values were less than 0.01 (**: $p < 0.01$), 0.001 (***: $p < 0.001$), or 0.0001 (****: $p < 0.0001$). All results were represented or plotted as the mean ± standard deviation.

https://doi.org/10.1021/acsami.1c16307
ACS Appl. Mater. Interfaces 2022, 14, 104−122

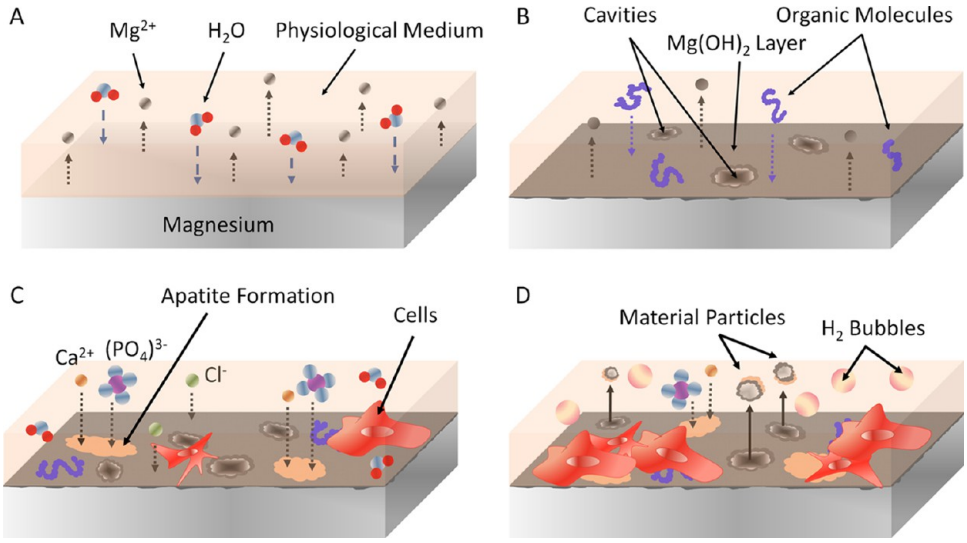

Figure 2. Schematic representation of the biocorrosion of magnesium under physiological conditions. (A) Due to impurities and agglomerated cathodic phases on the grain boundaries, the magnesium matrix starts to undergo galvanic corrosion and Mg^{2+} ions are released. (B) Protective $Mg(OH)_2$ layer formation on the surface of the material. Organic molecules in the physiological medium adsorb onto this new surface, influencing the biocorrosion process. (C) Chloride ions in the physiological medium react with the protective $Mg(OH)_2$ layer, forming the highly soluble magnesium chloride. Magnesium chloride dissolves in the medium, creating cavities on the material surface (pitting corrosion). Calcium and phosphate ions in the medium form calcium phosphate deposits on the intact portions of the $Mg(OH)_2$ protective layer. Cells also adhere to the $Mg(OH)_2$ surface. (D) Cells attached to the surface of the material proliferate and form new tissue, while some magnesium particles break free from the bulk magnesium matrix.

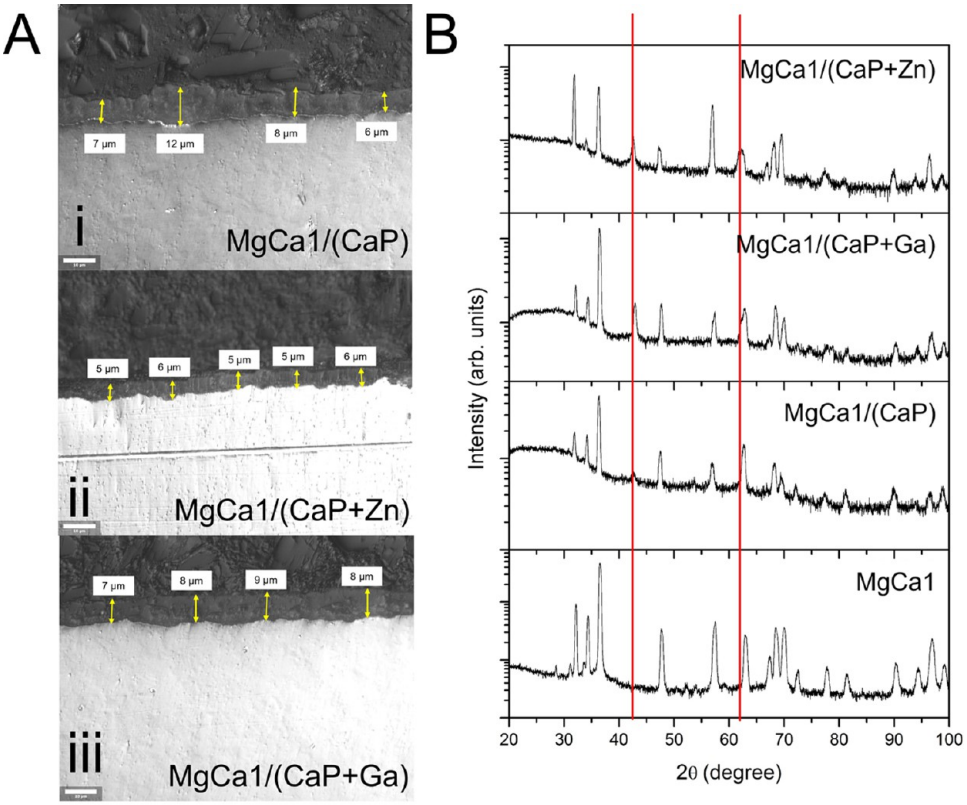

C

Sample	MgCa1/(CaP)	MgCa1/(CaP+Zn)	MgCa1/(CaP+Ga)
Ca/P Ratio	0.34 ± 0.03	0.21 ± 0.02	0.35 ± 0.03

Figure 3. Physical and chemical properties of coatings. (A) Cross-sectional images of MgCa alloys with various CaP-based coatings. (i) MgCa1/(CaP), (ii) MgCa1/(CaP+Zn), and (iii) MgCa1/(CaP+Ga). Yellow arrows indicate the coating thicknesses measured. Scale bars: 10 μm. (B) XRD diffractograms of the MgCa-based implant materials. (C) Ca/P ratios of the CaP-based coatings.

https://doi.org/10.1021/acsami.1c16307
ACS Appl. Mater. Interfaces 2022, 14, 104−122

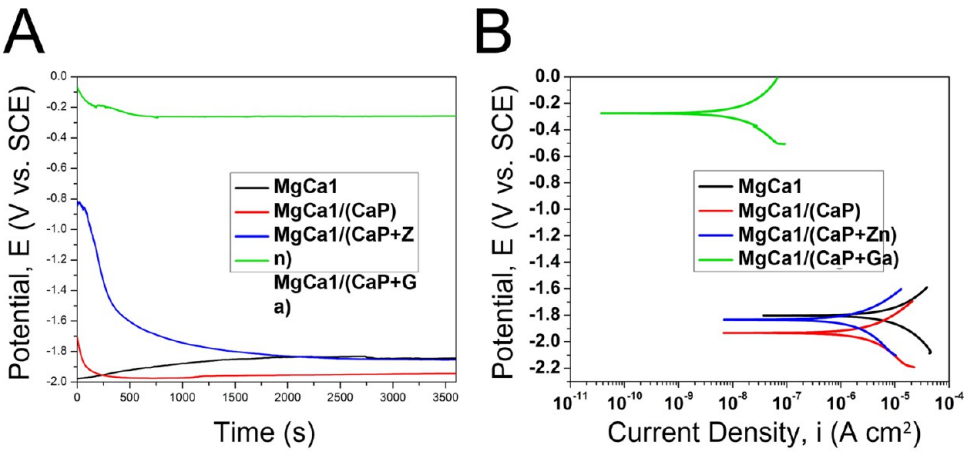

C

Sample	E_{oc} (mV)	E_{cor} (mV)	i_{corr} (μA cm^{-2})	R_p (kΩ cm^2)	P_e (%)
MgCa1	-1843	-1801	21.751	6	-
MgCa1/(CaP)	-1944	-1933	5.951	17	72.6
MgCa1/(CaP+Zn)	-1854	-1833	3.269	32	85.0
MgCa1/(CaP+Ga)	-258	-275	0.065	3917	99.7

Figure 4. Corrosion resistance results of the specimens. (A) Evolution of the open-circuit potential in time, (B) Tafel plots, and (C) main corrosion parameters (E_{oc}, open-circuit potential; E_{cor}, corrosion potential; i_{corr}, corrosion current density; R_p, polarization resistance; P_e, protection efficiency at the corrosive attack).

3. RESULTS AND DISCUSSION

Preparation of biodegradable metallic implants for use in medical applications is a very challenging subject.[15,16] The most commonly used biodegradable alloys are based on Mg.[7,9,20] Degradation of pure Mg is a fast process, leading to formation of ions, production of hydrogen gas, and eventually protein adsorption and cell adhesion in the physiological environment (Figure 2). In this study, magnesium−calcium alloys (MgCa1) were modified with calcium phosphate (CaP) coatings doped with zinc (Zn) or gallium (Ga) via microarc oxidation. Phase composition, adhesion, wettability, and mechanical properties of the coatings and corrosion resistance were investigated after surface modifications. Indirect cytotoxicity and cell viability were evaluated with L929 cells and Saos-2 cells, respectively. Topographical and morphological analyses were conducted with profilometry, SEM, and EDS before and after cell culture experiments.

3.1. Physical, Chemical, and Mechanical Characterizations. *3.1.1. Thickness, Phase Composition, and Ca/P Ratio of the Coatings.* Cross sections of the MgCa alloys with CaP-based coatings are presented in Figure 3A. All three coatings exhibited the typical two-layer morphology of MAO coatings with a compact inner layer that strongly adheres to the substrate and an outer layer that is microporous in nature due to the microarc oxidation process.[62,63] The coating thickness was nonuniform for the undoped CaP coating (Figure 3A,i) compared to the Zn- (Figure 3A,ii) and Ga-doped (Figure 3A,iii) coatings. The average coating thickness values were 8.25 ± 2.63, 5.40 ± 0.55, and 8.00 ± 0.82 μm for CaP, CaP+Zn, and CaP+Ga, respectively. Coating thicknesses from 1 to 16 μm are reported in the literature with the MAO method.[62−65] CaP+Zn was the most compact among all coatings and exhibited an organized, columnar cross-sectional morphology with rodlike deposition patterns (Figure 3A,ii), while undoped and Ga-doped coatings exhibited an unorganized deposition pattern.

XRD diffractograms for modified surfaces and uncoated MgCa1 alloy as control group are presented in Figure 3B. Coatings exhibited almost the same peaks as the substrate in the diffractogram, rendering it difficult to differentiate the peaks of the coating from those of the substrate. According to the standard ICDD#03-065-3583, formation of the magnesium carbide (Mg_2C) phase can be observed from the peaks located at 28.68, 31.25, 33.5, and 52.24°. Consistent with ICDD#01-071-3765, the peaks located at 32.16, 34.49, 36.63, 47.93, 57.50, and 63.16° are attributed to Mg. The peak located at 36.63° associated with Mg is also visible after coating deposition. The peak located at 32.16°, which has a similar position to the Mg alloy, can be related to the formation of the CaP phase on the substrate based on the changes in the peak intensity. According to the ICDD#09-0432 standard, the CaP phase has the same peaks as the uncoated MgCa substrate. However, two peaks, located at 42.47 and 61.87°, are attributed to CaP only. The changes in the intensity of these two peaks for coated samples indicate successful alteration of the substrate surface with the CaP phase. The peak located at 42.47° has a higher intensity for Zn- and Ga-doped coatings compared to the undoped CaP coating. For the doped coatings, no peaks of dopants were detected. This is due to the similarities between the peaks of the uncoated substrate and those of coatings and dopants. However, XRD patterns of doped coatings are slightly distorted compared to those of the undoped CaP, indicating that the dopants are present in the sample.

https://doi.org/10.1021/acsami.1c16307
ACS Appl. Mater. Interfaces 2022, 14, 104−122

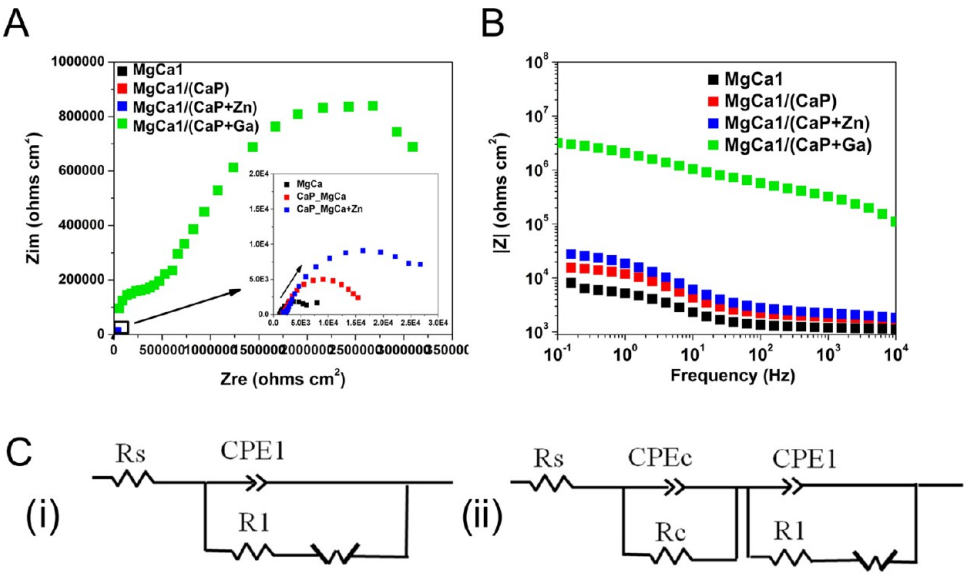

D

	MgCa1	MgCa1/(CaP)	MgCa1/(CaP+Zn)	MgCa1/(CaP+Ga)
R (Ω cm²)	1.12E+03	1.61E+03	1.16E+03	1.64E+03
Y_c (μΩ^{-1} cm^{-2} s^n)	-	1.13E+01	8.72E+00	1.50E-01
n_c	-	8.60E-01	7.60E-01	4.80E-01
R_c (Ω cm²)	-	1.11E+04	2.69E+04	4.13E+06
Y_1 (μΩ^{-1} cm^{-2} s^n)	3.91E+01	2.86E+02	1.10E+01	2.00E-04
N_1	5.90E-01	2.90E-01	3.70E-01	9.90E-01
R_1 (Ω cm²)	2.30E+02	2.00E-04	4.30E-03	2.01E+05
W (Ω cm² s^n)	6.32E+03	2.58E+04	1.35E+03	1.20E+05
X^2	6.90E-04	1.06E-03	6.50E-04	4.40E-04

Figure 5. Electrochemical impedance spectroscopy results for MgCa-based materials. (A) Nyquist and (B) Bode plots for the samples investigated. (C) Electrical equivalent circuit models used for fitting: (i) model representing uncoated MgCa1 as the substrate and (ii) model representing CaP-coated variants as the substrate. (C) EIS data of the samples investigated after fitting.

Using the peak located at 42.47° attributed to the CaP phase, which appeared after the coating process, the grain size was calculated according to the Scherrer formula.[66] The results showed that undoped CaP has a grain size of 43.1 nm, while Ga- and Zn-doped CaP coatings have grain sizes of 58.1 and 28.2 nm, respectively.

The Ca/P ratios of all CaP-based coatings prior to corrosion testing are presented in Figure 3C. Ca/P ratios varied between 0.21 and 0.35 for all samples, which are considerably lower than that of the stoichiometric hydroxyapatite (1.67).[67]

3.1.2. In Vitro Corrosion Resistance. The change in the open-circuit potential during the immersion of samples in Dulbecco's modified Eagle's medium (DMEM) solution was recorded for 1 h (Figure 4). The curves obtained for the coated samples were similar, with more electropositive values being recorded at the beginning of the test. After a quick decrease, the potential was stabilized, and all specimens reached a steady-state value at the end of the test. Different behavior was exhibited by uncoated MgCa1. The E_{oc} increased gradually for this sample, reaching a stable value of −1843 mV, followed closely by MgCa1/(CaP+Zn), whose E_{oc} value was −1944 mV (Figure 4C). However, a relatively high potential was observed for the coated sample doped with Ga, with the final E_{oc} being −258 mV.

Tafel plots in Figure 4B show that the samples exhibit different corrosion behaviors according to their composition. A more positive corrosion potential (E_{cor}) and lower corrosion current density (i_{corr}) was observed for the Ga-doped sample, an indicator of its effectiveness in enhancing the corrosion resistance. The rest of the samples showed corrosion behavior similar to uncoated MgCa1; however, they reached smaller values of i_{corr}.

All coated specimens displayed better corrosion resistance than the uncoated MgCa1 substrate, with MgCa1/(CaP+Ga) having the lowest value of corrosion current (i_{corr} = 0.065 μA·cm^{-2}) (Figure 4C), followed by MgCa1/(CaP+Zn) and MgCa1/(CaP).

The polarization resistance was calculated based on one form of the Stern−Geary equation using previously determined values of E_{cor}, i_{corr}, and Tafel slopes (β_a and β_c)

$$\frac{1}{R_p} = \left(\frac{\Delta i}{\Delta E}\right)_{E_{corr}} = 2.3\left(\frac{\beta_a + |\beta_c|}{\beta_a |\beta_c|}\right) i_{corr} \quad (1)$$

Considering the polarization resistance (R_p), corrosion resistance was in the decreasing order MgCa1/(CaP+Ga) > MgCa1/(CaP+Zn) > MgCa1/(CaP) > MgCa1.

The protection efficiency (P_e) was calculated taking into account the corrosion current values of the coated samples and the uncoated MgCa1[68,69] with the following formula

$$P_e = \left(1 - \frac{i_{corr\_coating}}{i_{corr\_substrate}}\right)\cdot 100 \quad (2)$$

https://doi.org/10.1021/acsami.1c16307
ACS Appl. Mater. Interfaces 2022, 14, 104−122

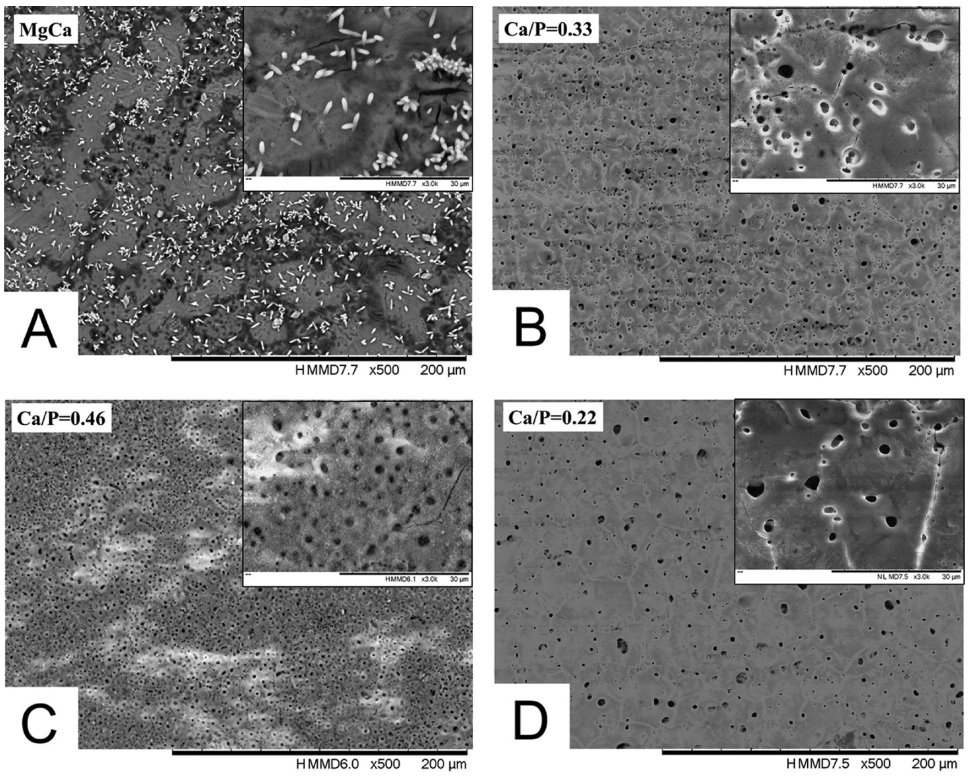

Figure 6. SEM micrographs of the specimens after the corrosion test. (A) MgCa1, (B) MgCa1/(CaP), (C) MgCa1/(CaP+Zn), and (D) MgCa1/(CaP+Ga). Scale bars, 500×−200 μm; Insets, 3000×−30 μm.

The results show that by Zn and Ga addition into CaP composition, the protection efficacy was increased, reaching a value of P_e = 99.7%, the highest among coated variants, in the case of MgCa1/(CaP+Ga) (Figure 4C).

The results of electrochemical impedance spectroscopy for the MgCa-based samples are shown in Figure 5. The diameter of the semicircle obtained in the Nyquist plot is related to the corrosion resistance of the sample, and the shape of the experimental data gives an insight into the electrochemical reactions happening during the EIS analysis (Figure 5A). Nyquist and Bode plots show a clear trend of corrosion resistivity for the samples: MgCa1/(CaP+Ga) > MgCa1/(CaP+Zn) > MgCa1/(CaP) > MgCa1. Moreover, a significant difference was observed between the Ga-doped, CaP-coated sample and the rest of the analyzed samples, where the |Z| values recorded show more than one order of magnitude of difference (Figure 5B).

Data obtained from EIS measurements were fitted using an equivalent circuit model (EEC), as presented in Figure 5C. It represents the solution for both uncoated MgCa1 and the coated samples. Rs stands for the solution resistance and CPE denotes a constant-phase element (characterized by the admittance Y_0 and power index number n, as follows: $Y = Y_0(j\omega)^n$). The value of n may differ; when $n = 1$, the CPE behaves like an ideal capacitor.[70] In the case of $n < 1$, which represents our system, a CPE that considers the deviation from the ideal dielectric behavior is used and it is related to surface inhomogeneity. The model shown in Figure 5C,i represents uncoated MgCa used as the substrate. In this case, CPE1 and R1 parameters represent the double electric layer capacitance and charge-transfer resistance, respectively, and are used to characterize the electrode−solution interface. The EEC proposed for the CaP-coated variants is shown in Figure 5C,ii, where CPEc and R_c represent the capacitance and resistance of the CaP coating (with or without Zn and Ga doping), respectively. In this case, R_c is used to simulate the resistance associated with the current flow through the pores generated by the coating defects. The Warburg element (W) was added to electrical equivalent circuits used for fitting the obtained impedance data to investigate the diffusion process across the investigated interface. The Warburg impedance was used as an insight into the presence of mass-transfer reactions. Low χ^2 values obtained indicate good fitting for all models (Figure 5D).

The main parameters describing the electrochemical behavior of samples during EIS measurements are presented in Figure 5D. There is a certain tendency regarding the coated specimens when it comes to capacitive response; Y_c decreased from 11.29 Ω^{-1} cm^{-2} s^n for MgCa1/(CaP) to 8.72 Ω^{-1} cm^{-2} s^n for the Zn-doped sample, and an even greater decrease to 0.15 Ω^{-1} cm^{-2} s^n was observed for the Ga-doped sample. The same trend was observed for Y_1, which characterizes the electrolyte−substrate interface (Figure 5D). The results indicated better protection of the deposited coating for the MgCa1/(CaP+Ga) sample, followed by MgCa1/(CaP+Zn) and MgCa1/(CaP).

The resistance associated with the coatings (R_c) reached a higher value for MgCa1/(CaP+Ga), suggesting that this specimen had the least number of defects. This finding can also be attributed to the roughness since there is a drop regarding n_c for CaP+Ga/MgCa1 (Figure 5D). This gives an indication of the nature of the coatings and their nonideal character, with the lowest dispersion being observed in the case of CaP/MgCa1 (n_c = 0.86). However, at the interface with the substrate, there is an indirect phenomenon; the higher the n_c value is, the lower the n_1 becomes. MgCa1/(CaP+Ga) was the least affected by this phenomenon among the coated variants, with an n_1 value even higher than the uncoated MgCa1 sample

https://doi.org/10.1021/acsami.1c16307
ACS Appl. Mater. Interfaces 2022, 14, 104−122

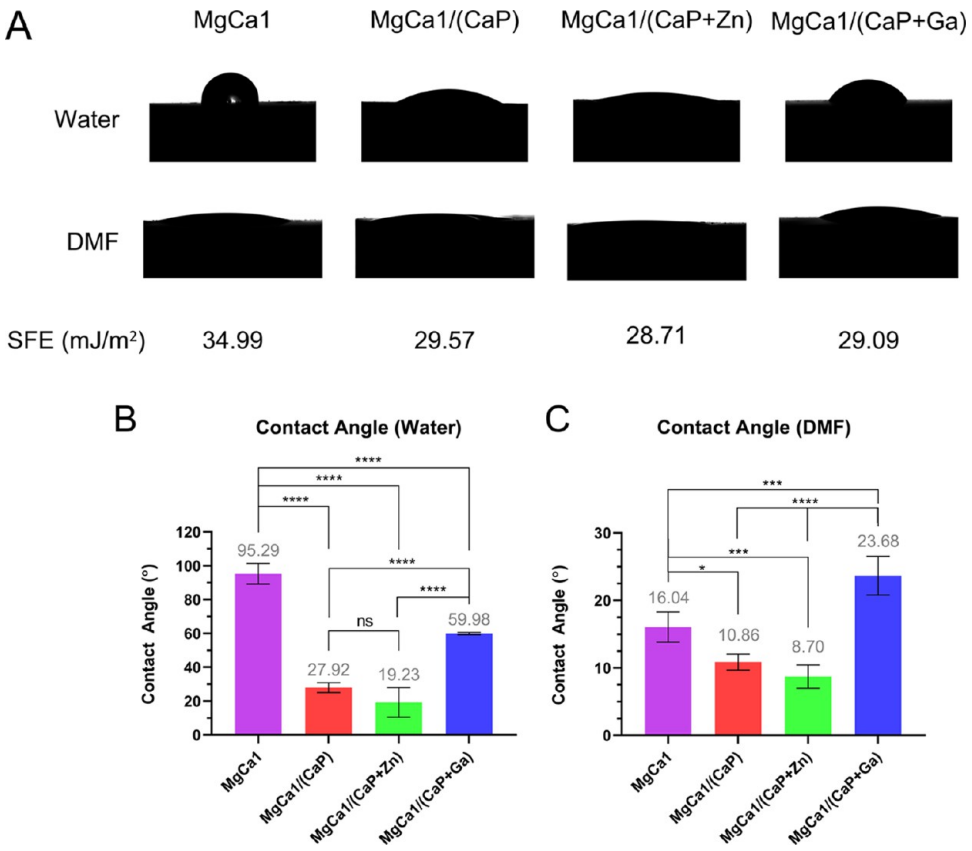

Figure 7. Contact angle and surface free energy (SFE) measurements for MgCa1-based implant materials. (A) Images of contact angles obtained with water and DMF, and the SFE values obtained via the Zisman method. (B) Water contact angles, and (C) *N*,*N*-dimethylformamide (DMF) contact angles of Mg-based alloys.

(Figure 5D). These deviations in n values arise either from the differences in properties along the surface of an electrode (e.g., roughness) or properties normal to the surface (e.g., thickness).[71]

The charge-transfer resistance (R_1) was higher for uncoated MgCa1 compared to that for the coated samples, except for MgCa/(CaP+Ga) (Figure 5D). The Warburg impedance (W) parameter also indicated that Ga-doped coating had the best resistance when it comes to mass-transfer reactions.

The corrosion process in the human body is more complex as compared to that in a simple salt solution since blood plasma and intracellular fluid contain a variety of organic compounds in addition to the inorganic ions (Mg^{2+}, Ca^{2+}, Cl^-, HCO_3^-, etc.).[72] However, simulated body fluid (SBF) could not be used in corrosion testing because calcium carbonate clusters formed after immersion of samples in SBF for 1 day, which would obviously complicate the results.[73] Furthermore, DMEM provided a better test environment compared to SBF, phosphate-buffered saline (PBS), or Hank's balanced salt solution (HBSS) as this cell culture medium contains amino acids, minerals, glucose, and vitamins that help better simulate the physiological environment.[74] The high resistance to corrosion of our samples in DMEM could be related to the development of a protective layer on top of the examined surfaces by adsorption of these proteins and other organic elements from the DMEM composition. A similar finding was reported by Popa et al. in the case of bioglass coatings.[75] In addition, DMEM simulates a stable physiological pH and has been reported to lead to a degradation rate and a degradation layer similar to that obtained under *in vivo* conditions.[76]

It was reported that the corrosion rates of Zn-doped magnesium in the minimum essential medium (MEM) and in MEM-containing 40 g/L bovine serum albumin (MEMp) were 0.959 mm/year and 1.716 mm/year, respectively, while it was much lower, 0.378 mm/year, in vivo.[77] Wan et al. showed that zinc addition to Mg increases corrosion, and it was concluded that zinc was not a favorable element for Mg modification in biomedical applications.[43] Our results show that although Zn-doped coatings improve corrosion resistance compared to the uncoated MgCa1 substrate, the effect of Zn doping is not significant compared to the undoped CaP coating. Meanwhile, Ga doping has significantly improved the corrosion resistance of the CaP coating applied, which is in accordance with the literature.[78]

Surface morphologies of the samples after the corrosion test are presented in Figure 6. Micron-sized, mainly Ca-based flakes, appeared on the surface of uncoated MgCa1 after the corrosion test (Figure 6A). The origin of these flakes on the sample surface is attributed to the $CaCl_2$ content in the DMEM solution used during the test. It is understood that a uniform oxidative process was maintained during corrosion testing since oxygen (O) was present in the EDS spectra of all specimens (data not shown). At higher magnifications, a clear deterioration of the coarse structure of the coatings is visible due to the corrosion process. The MgCa1/(CaP) sample had the most homogeneous surface, which changed into a surface with more pronounced features with the addition of dopants Zn and Ga. Ca/P ratios of the coatings after corrosion testing varied between 0.22 and 0.46 (Figure 6B–D).

https://doi.org/10.1021/acsami.1c16307
ACS Appl. Mater. Interfaces 2022, 14, 104−122

A

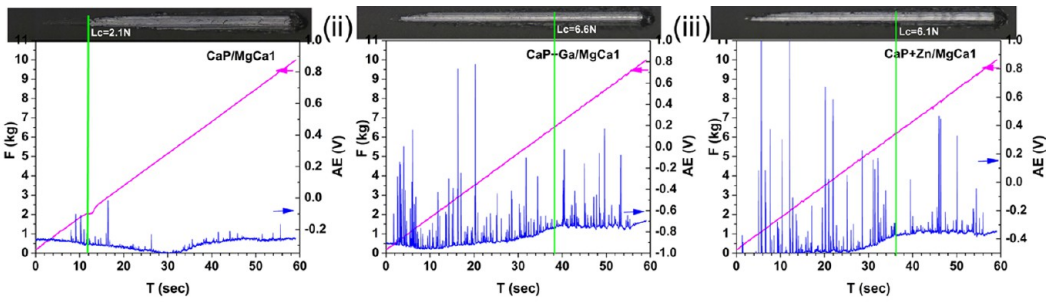

B

Sample	H (GPa)	E (GPa)	H/E	H/ E^2	H^3/E^2	L_c
MgCa1/(CaP)	4.58 ± 0.20	81.90 ± 1.30	0.056	6.83E-4	0.0143	2.10 ± 0.20
MgCa1/(CaP+Zn)	1.62± 0.10	60.00 ± 5.00	0.027	4.50E-4	0.0011	6.10 ± 0.30
MgCa1/(CaP+Ga)	3.34± 0.10	67.90 ± 10.00	0.049	7.24E-4	0.0080	6.50 ± 0.30

Figure 8. Mechanical testing of the CaP-based coatings. (A) Acoustic emissions from the scratch testing and the resulting scratch force versus time graphs for CaP coatings. (B) Elastic modulus (E); hardness (H); H/E, H/E^2, and H^3/E^2 ratios; and critical load (L_C) values calculated for different coating types.

3.1.3. Wettability and Surface Free Energy. Surface wettability and, by extent, surface free energy (SFE) are important parameters that determine the degree of affiliation of an implant material with host cells and tissues and the physiological environment, affecting the host response to implantation.[79] Surface wettability influences protein adsorption and subsequently the adhesion and proliferation of preosteoblasts on implant surfaces.[80] Moderate wettability is advantageous for orthopedic implant materials in terms of cell attachment, proliferation, and mineralization of the implant surface.[81] The surface energy of the implant material is also important for mineralization.[82] Therefore, the wettability and surface energy of all samples were investigated. Contact angles of the samples were determined using water and *N*,*N*-dimethylformamide (DMF) as the contacting liquids (Figure 7A).

The water contact angle (WCA) of uncoated MgCa1 alloy was found to be 95.29 ± 6.12°, demonstrating a hydrophobic surface (Figure 7B). The WCA values decreased significantly for coated samples, indicating that a more hydrophilic material surface was achieved with the coatings. This considerable difference in wettability between uncoated and coated samples was ascribed to the increased surface roughness and the porous nature of the coatings.[80] MgCa1/(CaP+Zn) showed the highest surface wettability among the coated samples (WCA: 19.23° ± 8.69), followed by MgCa1/(CaP) (27.92° ± 2.90) and MgCa1/(CaP+Ga) (59.98° ± 0.69). All coated samples had WCA ≤ 60°, which generally favors the attachment of anchorage-dependent osteoblasts,[83] suggesting the surface-modified alloys would demonstrate good cell–material surface interactions.

Surface free energies of all samples were determined using the Zisman model. Zisman plots of the samples were constructed using the contact angles (θ) obtained with water (Figure 7B) and *N*,*N*-dimethylformamide (DMF) (Figure 7C). The SFEs obtained from Zisman plots are presented in Figure 6A. Coated samples had lower values of SFE compared to the uncoated alloy. Meanwhile, among the coated variants, doping with Zn or Ga did not cause a significant change in the SFE values. This finding is attributed to the similarities between the properties of the dopants Zn and Ga (atomic numbers 30 and 31 and electronegativity values 1.65 and 1.81, respectively). Studies show that cell adhesion improves with increasing SFE[84] and osteoblast differentiation is promoted on materials with high SFEs.[85] However, morphological features such as roughness and porosity are known for having a more prominent effect on cell adhesion and proliferation than the SFE profiles.[84,85]

3.1.4. Mechanical Testing of the Coatings. 3.1.4.1. Hardness and Elastic Modulus. Hardness (H) and elastic modulus (E) values of the CaP coatings were determined using a nanoindenter system with the Oliver–Pharr method. Dopant addition was shown to decrease the hardness of the coatings, the effect being most evident for the Zn-doped CaP coatings. The MgCa1/(CaP) sample presented the highest hardness value, followed by MgCa1/(CaP+Ga) and MgCa1/(CaP+Zn) (Figure 8). A similar trend was observed for the elastic modulus. However, no significant difference was observed between the E values of Ga- or Zn-doped CaP coatings. The resistance to plastic deformation, represented by the H^3/E^2 ratio, was higher for undoped CaP coating, indicating a better toughness compared to the Zn- and Ga-doped coatings. However, the H/E ratio, which characterizes brittleness, was lower for Zn- and Ga-doped variants, meaning that a less brittle coating was achieved with doping. The wear resistance of the coatings, indicated by the H/E^2 ratio, was greater for Ga-doped CaP coating compared to that for other variants. Meanwhile, undoped CaP coating performed better than the Zn-doped coating in this regard.

Zn doping is shown to improve the surface hardness and modulus for Mg alloys in the literature, which was not in accordance with the results obtained in this work.[43,86] However, it should be noted that these results depend heavily on the composition of the alloys, composite preparation technique, homogeneity, and grain size.

3.1.4.2. Coat Adhesion. The adhesion strength of the CaP-based coatings to the MgCa1 substrate was investigated by scratch tests (Figure 8). The undoped CaP coating exhibited poor adhesion to the MgCa1 substrate, while the Ga-doped coatings showed higher adhesion, followed closely by Zn-doped CaP coatings (Figure 8A). Delamination of the undoped CaP coatings from the MgCa1 substrate surface started around 2 N, while for Zn- and Ga-doped coatings, delamination started after the application of a force of 6 N (Figure 8B).

It is important for CaP-based coatings to display and maintain strong adhesion to the MgCa1 substrate, as this will affect the resulting implant material's ability to sustain resistance to corrosion under physiological conditions. Coating adhesion is strongly dependent on the surface properties of the substrate.

https://doi.org/10.1021/acsami.1c16307
ACS Appl. Mater. Interfaces 2022, 14, 104–122

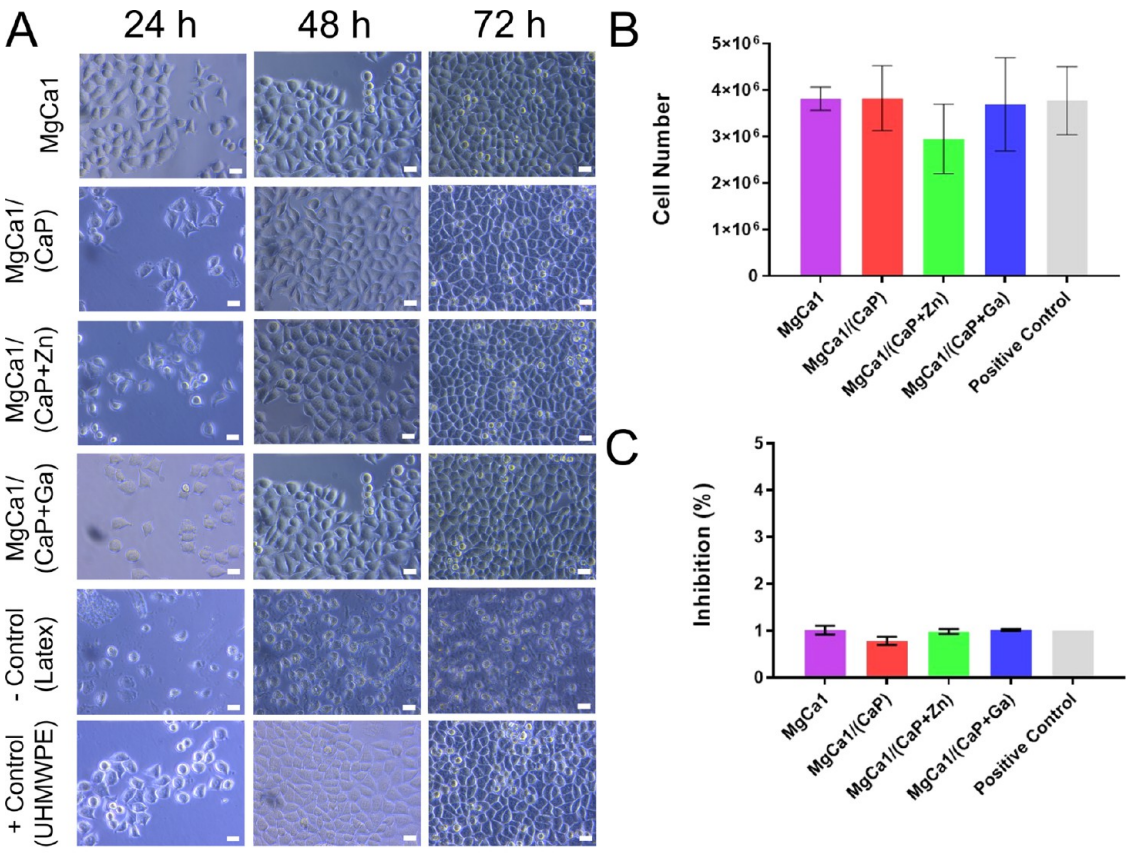

D

A: Scoring and evaluation according to ISO 10993/EN 30993						
Cell confluency (%) [A]		100	90-100	60-90	30-60	0-30
	Score:	0	1	2	3	4
Dead cells (%) [B]		No cells	0-5	5-10	10-20	≥20
	Score:	0	1	2	3	4
Morphological Change [C]		No change in any cell	Change only in few cells	Less than half of the cells	More than half of the cells	Almost all cells
	Score:	0	1	2	3	4
Inhibition of Cell Growth (%) [D]		0-10	10-30	30-50	50-70	70-100
	Score:	0	1	2	3	4
Cytotoxicity Index**		0-3		3-5		5-8
	Indication:	Cytocompatible		Additional Evaluation Required		Cytotoxic

B: Evaluation of cytotoxicity of the samples treated with L929						
Sample	Confluency [A]	Dead Cells [B]	Morphological Change [C]	Inhibition of Cell Growth [D]	Cytotoxicity Index**	Cytotoxicity
MgCa1	1	1	1	0	1	No
MgCa1/(CaP)	1	1	1	0	1	No
MgCa1/(CaP+Zn)	1	1	1	0	1	No
MgCa1/(CaP+Ga)	1	1	1	1	2	No

Figure 9. Indirect cytotoxicity test results. (A) Morphology of L929 cells after 24, 48, and 72 h treatment with the sample, positive control, and negative control extracts under a light microscope (×40). About 10^4 cells were seeded in each well initially. Latex was used as the negative control, and ultrahigh molecular weight poly(ethylene) (UHMWPE) was used as the positive control. Scale bars: 20 μm. (B) Number of viable cells after 72 h treatment of L929 cells with extracts of the implant materials, compared to the positive control. (C) Inhibition (%) of cell growth (based on the negative control, latex, taken as 100%) for each sample group. (D) Part A, indirect cytotoxicity evaluation according to ISO 10993/EN 30993*; and Part B, scores of the samples after culturing L929 cells with their extracts for 72 h. (*Extract of samples and controls obtained in DMEM high culture media were used to treat L929 cells. **Cytotoxicity Index is calculated by taking the average of the scores obtained from the first three observations ($^{A, B, C}$) and adding this value to the score of the fourth observation (^{D}).).

The strongest adhesion to the MgCa1 alloy was observed in the case of Ga-doped CaP coating, which also exhibited good mechanical properties.

3.2. Cytotoxicity, Cell Viability, and Cell−Substrate Interaction on Implant Materials. *3.2.1. Indirect Cytotoxicity Tests.* For indirect cytotoxicity testing, extracts of Mg-based samples were obtained by immersion in DMEM high-glucose

https://doi.org/10.1021/acsami.1c16307
ACS Appl. Mater. Interfaces 2022, 14, 104−122

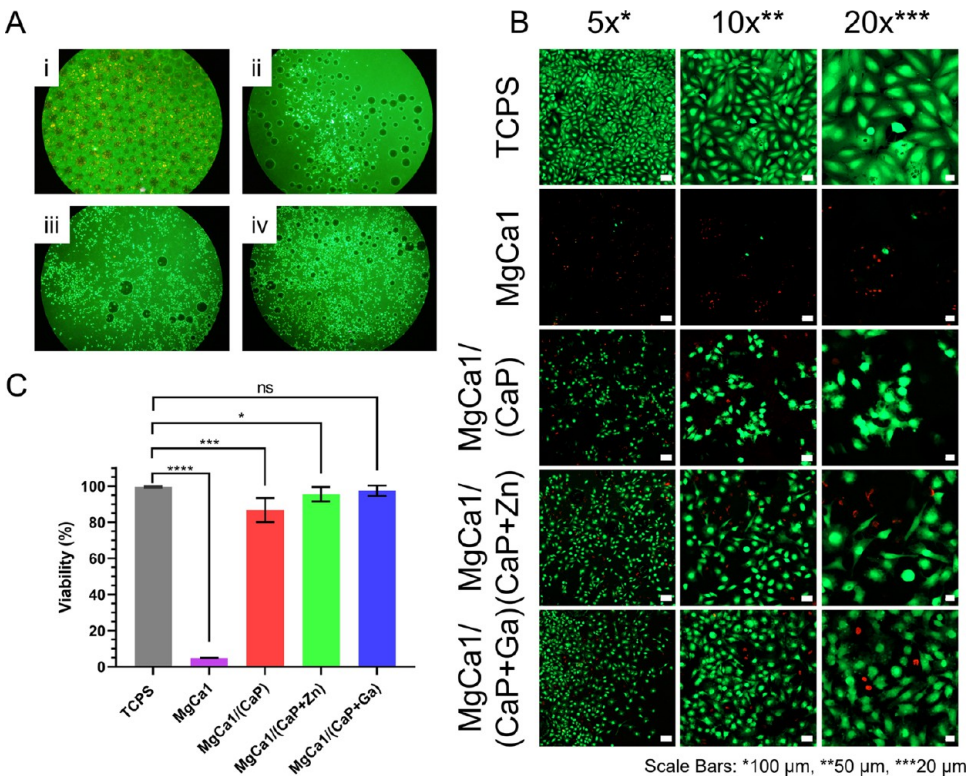

Figure 10. H_2 gas release from the samples and live−dead (viability/toxicity) evaluation of Saos-2 cells cultured on samples on day 2. (A) Micrographs taken directly from the eyepiece of the CLSM showing H_2 gas bubbles released from different MgCa1 samples after 2 days in cell culture media: (i) MgCa1 (control), (ii) MgCa1/(CaP), (iii) MgCa1/(CaP+Zn), and (iv) MgCa1/(CaP+Ga). (B) CLSM micrographs of Saos-2 cells on different implant materials, costained with Calcein-AM and ethidium homodimer-1 dyes of the live−dead viability/cytotoxicity kit (green, Calcein-AM—live; red, ethidium homodimer-1—dead). (C) Quantification of Saos-2 cell viability on implant materials. Viability data is an average of live cells in the total cell number, obtained from three different regions of interest of three different biological repeats with CLSM (ns, not significant, $*p \leq 0.05$, $***p \leq 0.001$, $****p \leq 0.00001$). TCPS was the control (green, live; red, dead). (Scale bars: 5×−100 μm, 10×−50 μm, and 20×−20 μm).

cell culture medium for 24 h. The L929 fibroblast cell line was then treated with these extracts. The confluency, percentage of dead cells, morphological changes, and inhibition of cell growth were evaluated after treatment with extracts (Figure 9). Cells treated with the extracts of negative control (latex) showed circular morphology, while those treated with the positive control (UHMWPE) exhibited elongated morphology and good spreading, similar to the reports in the literature.[87] Cells treated with the extracts of different Mg-based samples were similar in morphology to those treated with the positive control, demonstrating proper spreading (Figure 9A). AlamarBlue tests showed that there was no significant decrease in the viable cell numbers and no significant increase in growth inhibition compared to the positive control after 72 h of incubation with material extracts (Figure 9B). Cells treated with the extracts of samples had about 1% growth inhibition (Figure 9C).

Indirect cytotoxicity evaluation was performed according to ISO 10993/EN 30993, which scores the cell behaviors in the range of 0−4 (Figure 9D—Part A). Each sample extract investigated had a cytotoxicity index of 1 or 2 based on the scoring guide, indicating that all samples were cytocompatible (Figure 9D—Part B). Alloys with certain soluble elements such as calcium, zinc, strontium, and zirconium and alloys with some rare-earth elements such as Mg-Y, Mg-Nd, and Mg-Dy with concentrations of 1−3% are shown to exhibit acceptable cytotoxicity.[88] Gu et al. examined the indirect cytotoxicity of binary Mg alloys prepared with different elements such as Al, Ag, In, Mn, Si, Sn, Y, Zn, and Zr with either cast or rolling processes, and observed no toxicity for Mg−Al, Mg−Sn, and Mg−Zn alloys against fibroblasts (L929 and NIH3T3 cell lines) and osteoblasts (MC3T3-E1 cell line).[30] One study by Si et al. recently demonstrated the positive effects of gadolinium (Gd) and zinc (Zn) in Mg−Zn−Gd alloy membranes on guided bone regeneration for rabbit calvarial defects.[89] Meanwhile, none to low cytotoxic effect and improvement of corrosion resistance for Mg alloys modified with lower concentrations of gallium (Ga) are available in the literature, although Ga is known as one of the bone resorption inhibitors.[41,90]

3.2.2. Cell Viability and Cell−Material Interactions. Cell viability and cell−substrate interactions on uncoated and surface-modified MgCa1 samples were studied with human osteosarcoma cell line Saos-2. Culture media of all samples showed a significant increase of pH toward the alkaline region on day 2, indicated by the color change of phenol red in the culture media to a bright pink compared to the yellowish color in the control group (TCPS). This was attributed to the hydrogen ions in the cell media being depleted by the production and release of H_2 gas as a direct result of the reaction between magnesium alloy and aqueous cell media.[91] Consequently, an accumulation of H_2 gas bubbles was present within the wells (Figure 10A). Furthermore, a continuous release of H_2 gas was observable under a microscope, either from large cavities present on the surface of the uncoated MgCa1 alloy (Supplementary Video) or from indentations at the edges where the integrity of the CaP-based coatings was disturbed in coated samples, although gas

https://doi.org/10.1021/acsami.1c16307
ACS Appl. Mater. Interfaces 2022, 14, 104−122

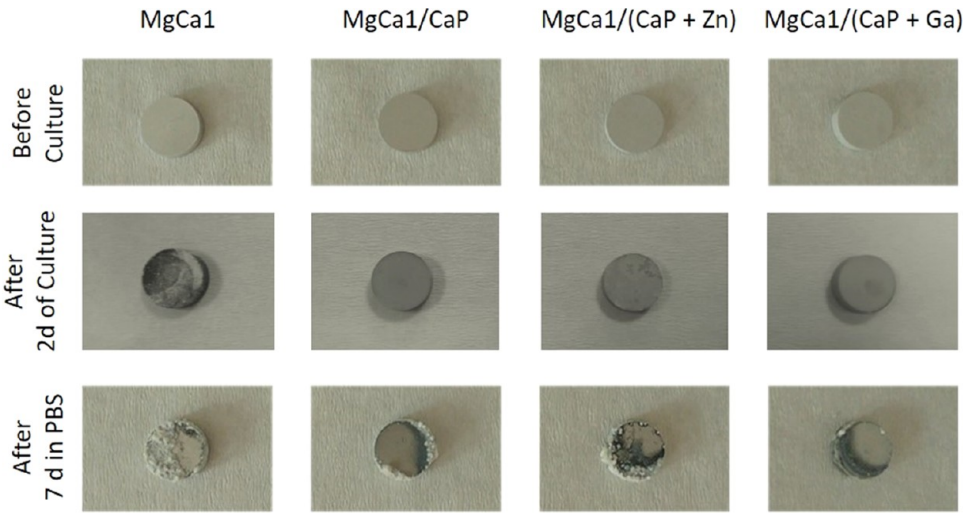

Figure 11. Mg-based implant materials before and after 2 days of culture with Saos-2 cells and after 7 days in PBS following 2 days of cell culture. Size of samples: diameter, 15 mm; thickness, 3 mm.

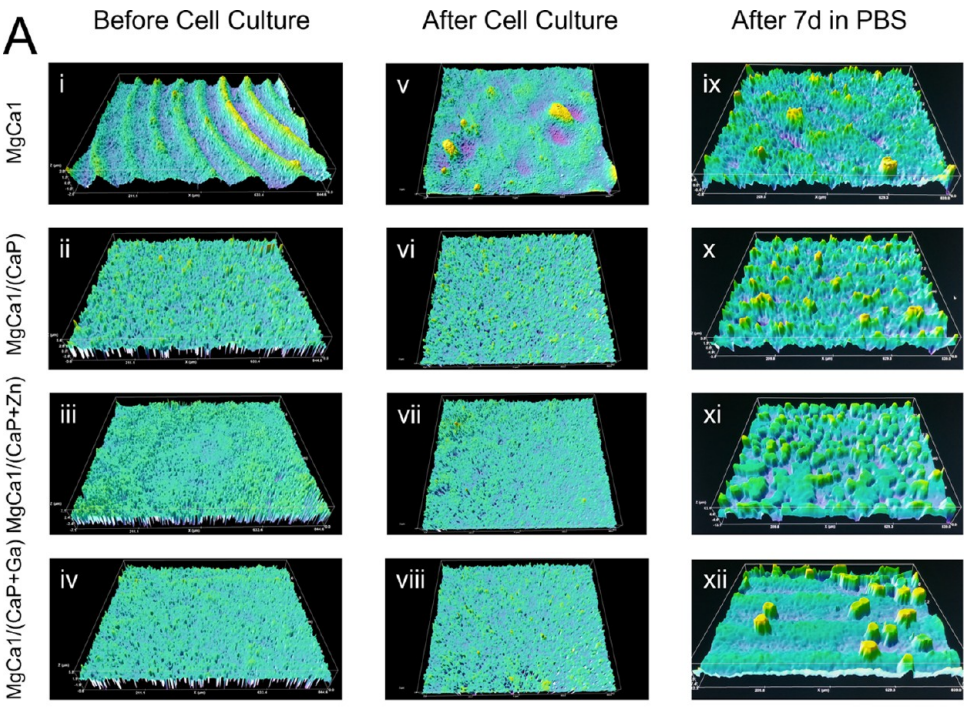

B

Property	Sq (μm)		Sa (μm)	
Sample	Before Cell Culture	After Cell Culture	Before Cell Culture	After Cell Culture
MgCa1	0.537 ± 0.209	0.720 ± 0.155	0.413 ± 0.163	0.446 ± 0.076
MgCa1/(CaP)	1.899 ± 0.061	1.718 ± 0.428	1.244 ± 0.056	1.219 ± 0.262
MgCa1/(CaP+Zn)	2.403 ± 0.130	2.481 ± 0.247	1.761 ± 0.476	2.030 ± 0.326
MgCa1/(CaP+Ga)	2.147 ± 0.536	1.880 ± 0.276	1.298 ± 0.243	1.109 ± 0.148

Figure 12. Surface profilometry analysis of MgCa1-based materials. (A) Surface topographies before (i, ii, iii, iv) and after (v, vi, vii, viii) 2 days of Saos-2 cell culture and after fixation with 4% paraformaldehyde and storage in PBS for 7 days (ix, x, xi, xii). (B) Surface roughness values of MgCa1-based implant materials before and after 2 days of cell culture (Sq, root mean square of heights; Sa, arithmetical mean deviation of the assessed profile; $N = 3$).

release in the latter was minimal and most likely a result of handling.

Samples were compared in terms of cell viability, attachment, and morphology (Figure 10B). On uncoated MgCa1 samples, nearly all of the cells seeded were detached from the surface or were dead, presumably due to the considerable corrosion of the substrate with rapid H_2 gas release from surfaces, which is in agreement with the literature.[92] Moreover, cells were probably

https://doi.org/10.1021/acsami.1c16307
ACS Appl. Mater. Interfaces 2022, 14, 104−122

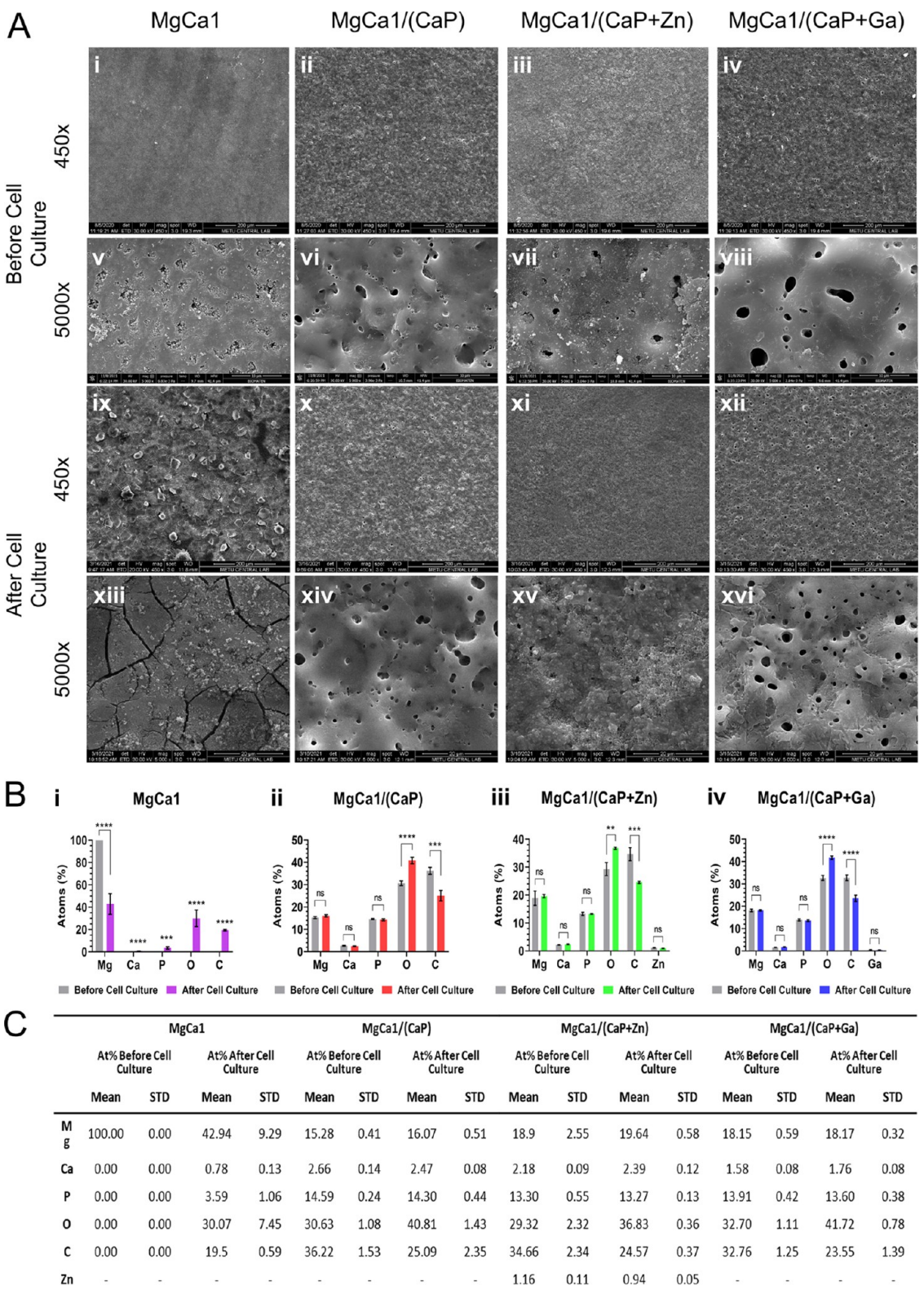

C

	MgCa1				MgCa1/(CaP)				MgCa1/(CaP+Zn)				MgCa1/(CaP+Ga)			
	At% Before Cell Culture		At% After Cell Culture		At% Before Cell Culture		At% After Cell Culture		At% Before Cell Culture		At% After Cell Culture		At% Before Cell Culture		At% After Cell Culture	
	Mean	STD	Mean	STD	Mean	STD	Mean	STD	Mean	STD	Mean	STD	Mean	STD	Mean	STD
Mg	100.00	0.00	42.94	9.29	15.28	0.41	16.07	0.51	18.9	2.55	19.64	0.58	18.15	0.59	18.17	0.32
Ca	0.00	0.00	0.78	0.13	2.66	0.14	2.47	0.08	2.18	0.09	2.39	0.12	1.58	0.08	1.76	0.08
P	0.00	0.00	3.59	1.06	14.59	0.24	14.30	0.44	13.30	0.55	13.27	0.13	13.91	0.42	13.60	0.38
O	0.00	0.00	30.07	7.45	30.63	1.08	40.81	1.43	29.32	2.32	36.83	0.36	32.70	1.11	41.72	0.78
C	0.00	0.00	19.5	0.59	36.22	1.53	25.09	2.35	34.66	2.34	24.57	0.37	32.76	1.25	23.55	1.39
Zn	-	-	-	-	-	-	-	-	1.16	0.11	0.94	0.05	-	-	-	-

Figure 13. Surface morphology and chemistry of MgCa1-based implant materials. (A) SEM micrographs before (i−viii) and after (ix−xvi) cell culture tests (scale bars: 450×−200 μm, 5000×—before culture, 10 μm; 5000×—after culture, 20 μm). (B) Change in the atomic proportion of elements on implant material surfaces upon cell culture according to EDS analysis: (i) MgCa1, (ii) MgCa1/(CaP), (iii) MgCa1/(CaP+Zn), and (iv) MgCa1/(CaP +Ga) (ns, not significant, $*p \leq 0.05$, $**p \leq 0.01$ $***p \leq 0.001$, $****p \leq 0.0001$). (C) Surface elemental compositions (atom %) of MgCa1-based implant materials from EDS analysis before and after cell culture.

stressed further in the newly formed highly alkaline environment, along with an increase in magnesium ion concentration within the culture media due to leaching, subsequently causing toxicity.[93] MgCa1/(CaP) samples had viable cells attached to the surface ($1.0 \times 10^3 \pm 4.4 \times 10^2$ cells/cm^2) compared to the uncoated MgCa1 that did not show any viable cell on the

https://doi.org/10.1021/acsami.1c16307
ACS Appl. Mater. Interfaces 2022, 14, 104−122

surface, suggesting a positive effect of CaP coating on cell affinity and survival (Figure 10B). Cell numbers on both surfaces, however, were less than that of the TCPS control. Cell morphology was also different from the control group; multiple filopodia were extended from the cells on the MgCa1/(CaP) sample surface. This is possibly a result of the constant probing of the substrate surface by the cells to find suitable sites to attach to. The numbers of cells attached to the surface of Zn- ($2.6 \times 10^4 \pm 6.5 \times 10^3$ cells/cm^2) and Ga-doped ($6.3 \times 10^4 \pm 1.6 \times 10^3$ cells/cm^2) coatings were higher than that on the surface of the undoped coating. Cell morphology on Zn- or Ga-doped coatings was similar to that of the control group. Disruption of coating integrity was lesser in the Zn- or Ga-doped coatings compared to that in the undoped CaP coating. This, in turn, minimized cell detachment from the surface and supported cell viability.

Cell viability was also quantified and presented as the percentage of live cells attached to the sample surface (Figure 10C). All coated samples performed better than the uncoated MgCa1 substrate in maintaining cell viability. The decreasing order of samples according to the number of viable cells attached to the surface is MgCa1/(CaP+Ga) > MgCa1/(CaP+Zn) > MgCa1/(CaP) > MgCa1 (Figure 10C). However, it should be noted that although MgCa1/(CaP) sample had a higher percentage of viable cells on its surface compared to the uncoated MgCa1 alloy, the total cell number was considerably lower than that of the TCPS control and the Zn- or Ga-doped samples.

3.2.3. Comparison of Surface Properties before and after Cell Culture. Samples were subjected to physical and chemical characterizations of the surface before and after cell culture with the Saos-2 cell line for 2 days and after 7 days immersion in phosphate-buffered saline (PBS, pH 7.4, 10 mM). Surface profilometry, goniometry, SEM, and EDS analyses were conducted for all samples. Figure 11 shows the implant materials before and after cell culture for 2 days and after 7 days in PBS upon fixation following culturing. A white deposit was observed after 2 days of cell culture on the surface of the uncoated MgCa1 sample, possibly due to the reactive nature of magnesium in the liquid media.[94] The coated samples did not exhibit such a deposit on their surface, presumably due to being shielded from cell culture media by the coatings. However, surfaces of all samples were covered with deposits after being immersed in PBS for 7 days following fixation with 4% paraformaldehyde solution. The amount of the deposit was the highest on uncoated MgCa1 and least on MgCa1/(CaP+Ga), consistent with the results of *in* vitro corrosion testing. Oxide layer formation on the surfaces was also observed as a change in the color of sample surfaces.[95] The effects of this reactivity on the chemical composition and physical properties of the samples were further investigated by profilometry, SEM, and EDS.

3.2.3.1. Surface Roughness. Changes in surface topography and roughness before and after cell culture were investigated for all samples (Figure 12A). The uncoated MgCa1 sample had regular undulations on its surface (Figure 12A,i) as a result of material processing, and these features were lost after cell culture for 2 days (Figure 12A,v). Roughness analysis showed no meaningful change in both the root mean square of heights (Sq) and arithmetical mean deviations of the assessed profiles (Sa) for this sample after cell culture (Figure 12B). This suggests that undulations were lost through excessive corrosion of the alloy surface in aqueous cell culture media, which formed corrosion pits that produced a similar roughness profile to the undulated alloy surface.

After CaP-based coating application, the undulated surface of MgCa1 alloy gave way to rough but leveled surfaces (Figure 12A,ii,iii,iv). Furthermore, coated samples had higher Sq and Sa values prior to cell culture compared to the uncoated MgCa1, suggesting successful alteration of the surface with the coating procedure (Figure 13B). Surface roughness values of Zn- or Ga-doped samples were higher than that of the MgCa1/(CaP) sample, which is due to the electrically conductive Zn^{2+} and Ga^{3+} ions increasing the reactive capacity of the electrolyte solutions used in the microarc oxidation (MAO) method, subsequently enhancing the deposition rate of the modified coatings.[96] All coated variants showed similar values of surface roughness before and after cell culture, indicating that the surface was not altered significantly for the duration of the cell culture studies.

After immersion in PBS for 7 days, all samples presented rougher surfaces with different geometries (Figure 12A). These new geometries were presumably a result of H_2 bubbles being trapped under the white deposits while Mg was reacting with aqueous PBS. This enhanced corrosion of the samples and alteration of surface morphology in PBS is largely attributed to the high chloride ion content of the buffer compared to that of the cell culture media, which is known to increase the corrosion rate of magnesium alloys.[31,97] Moreover, it should be remembered that the *in vitro* conditions are different than those in the *in vivo* environment, and the corrosion rate observed *in vivo* is generally lower than the corrosion rate under *in vitro* conditions due to the presence of organic components, such as proteins, which adsorb onto the material surface, forming a protective layer.[98]

3.2.3.2. Surface Morphology and Chemistry. **3.2.3.2.1. Surface Morphology**. Surface morphologies of Mg-based implant materials were observed before and after cell culture with Saos-2 cells for 2 days (Figure 13A). Uncoated MgCa1 alloy had undulations on its surface (Figure 13A,i), which were lost after cell culture (Figure 13A,ix), in accordance with the surface profilometry results. Higher magnifications show the extent of intergranular and pitting corrosion that took place on the uncoated alloy surface (Figure 13A,xiii). Prior to cell culture, coated samples were devoid of the undulations observed on the surface of the uncoated MgCa1 sample (Figure 13A,ii,iii,iv), and the coating was highly porous in nature (Figure 13A,vi,vii,viii). The micron-sized pores of the coatings form as a result of the molten oxide and gas bubble eruptions out of microarc discharge channels during the coating process.[99,100] After cell culture, these samples retained their porous surface morphology (Figure 13A,x,xi,xii). Higher magnifications reveal signs of erosion and microcrack formations on the surface; however, the integrity of the CaP coat is largely maintained (Figure 13A,xiv,xv,xvi). This retainment of coat integrity and porous surface morphology under an aqueous environment is advantageous in terms of cell attachment, tissue ingrowth, and interfacial fixation of the implant material to the bone tissue under physiological conditions.[6]

3.2.3.2.2 Surface Chemistry. Surface elemental compositions were determined for all sample groups before and after cell culture (Figure 13B,C). Traces of sodium (Na), potassium (K), and chlorine (Cl) were found on all sample surfaces after cell culture, possibly as salt depositions (Supplementary Figures S1−S4). The EDS spectrum of uncoated MgCa1 alloy was devoid of calcium (Ca), and after cell culture, traces of Ca and phosphorus (P) were found on this sample, possibly originating from the culture medium (Figures 13B,i and C). Meanwhile, a statistically significant increase in atomic percentages of oxygen

https://doi.org/10.1021/acsami.1c16307
ACS Appl. Mater. Interfaces 2022, 14, 104−122

(O) and carbon (C) was observed on the surface of the uncoated MgCa1 sample exposed to culture conditions, suggesting an oxidation reaction (MgO, CaO) or carbonate formation ($MgCO_3$, $CaCO_3$) taking place when the alloy was placed in the aqueous environment.[87] Another possible explanation for this increase would be serum protein deposition onto the material surfaces from the culture medium;[101] however, nitrogen (N) and hydrogen (H) signals were not detected from this sample. A similar increase in oxygen after cell culture was observed for CaP-coated (Figure 13B,ii), Zn-doped (Figure 13B,iii), and Ga-doped (Figure 13B,iv) samples, while the surface carbon content significantly decreased.

Atomic percentages (atom %) of the main alloy elements (Mg and Ca) were different for uncoated and coated samples prior to cell culture due to the introduction of Ca and P elements onto the alloy surface with coating applications. Meanwhile, atom % of Mg and Ca on all sample surfaces decreased proportionally after cell culture treatment, which is caused principally by the introduction of other elements (mainly C and O) to the material surface.

MgCa1/(CaP+Zn) samples contained 1.16 and 0.94% Zn, and MgCa1/(CaP+Ga) samples contained 0.49 and 0.45% Ga before and after cell culture, respectively (Figure 13C). In both cases, dopant atom % did not undergo a statistically significant change. Mg, Ca, and P elements followed the same trend for these samples, indicating that the composition of coatings and the underlying alloy was not significantly altered when subjected to culture conditions, which concurs with the surface morphology results from SEM.

4. CONCLUSIONS

Magnesium alloys are preferred biodegradable metals in medical applications, and the studies are concentrated on modifications of Mg alloys to control their degradation rates and enhance their biocompatibility. In this study, surfaces of MgCa1 alloys were modified with CaP coatings undoped or doped with Zn or Ga ions via the microarc oxidation technique. Uncoated MgCa1 samples corroded rapidly in the cell culture medium, while CaP-based coatings, especially those doped with Ga, had a significant protective effect against corrosion of the MgCa1 substrate, improving both cytocompatibility and cell viability. E_{corr} value increased from −1933 mV for CaP samples to more electropositive values of −275 mV for Ga-doped CaP coatings. Coating process created a rougher, porous, and more hydrophilic surface compared to the pristine alloy, promoting better cell attachment and growth. All samples were found to be cytocompatible. *In vitro* culturing of the samples with Saos-2 cells caused some variations in the elemental composition of the alloys due to their biodegradation. MgCa1/(CaP+Zn) samples contained 1.16 and 0.94 atom % Zn and MgCa1/(CaP+Ga) samples contained 0.49 and 0.45 atom % Ga before and after cell culture, respectively. The numbers of cells attached to the surface of Zn-doped (2.6×10^4 cells/cm^2) and Ga-doped (6.3×10^4 cells/cm^2) coatings were higher than that attached to the surface of the undoped coating (1.0×10^3 cells/cm^2). The adhesion of the CaP coating to the MgCa1 alloy substrate was improved by Ga and Zn additions. Zn and Ga doping also influenced the microstructure of the CaP coating, which in turn affected the mechanical properties. The hardness of the coating decreased from 4.58 GPa (CaP) to 1.62 GPa (CaP+Zn) and 3.34 GPa (CaP+Ga), while the elastic modulus decreased from 81.90 GPa (CaP) to 60 GPa (CaP+Zn) and 67.90 GPa (CaP+Ga), resulting in a material that could withstand plastic deformation during load bearing, similar to that observed with human joints. Adhesion of coating to the substrate was improved with Zn and Ga doping, and these variants showed minimal coat deformation under in vitro conditions, promising a sustainable corrosion protective effect in long-term use under physiological conditions. In conclusion, CaP-coated, Zn- and Ga-doped magnesium−calcium alloys developed in this study are novel and promising candidates as biodegradable metallic bone tissue implant materials in terms of corrosion resistance and osteoconductivity.

■ ASSOCIATED CONTENT

Supporting Information

The Supporting Information is available free of charge at https://pubs.acs.org/doi/10.1021/acsami.1c16307.

EDS spectra of MgCa1-based implant materials before and after cell culture (PDF)

Video showing H_2 gas bubble release from the uncoated MgCa1 sample (MP4)

■ AUTHOR INFORMATION

Corresponding Authors

Alina Vladescu − *National Institute of Research and Development for Optoelectronics - INOE 2000, Magurele 077125, Romania; Physical Materials Science and Composite Materials Centre, Research School of Chemistry and Applied Biomedical Sciences, National Research Tomsk Polytechnic University, Tomsk 634050, Russia;* orcid.org/0000-0001-5770-4541; Email: alinava@inoe.ro

Nesrin Hasirci − *BIOMATEN, Center of Excellence in Biomaterials and Tissue Engineering, Middle East Technical University (METU), Ankara 06800, Turkey; Department of Biotechnology, Middle East Technical University (METU), Ankara 06800, Turkey; Department of Chemistry, Middle East Technical University, Ankara 06800, Turkey; Tissue Engineering and Biomaterial Research Center, Near East University, 99138 Nicosia, Mersin 10, Turkey;* orcid.org/0000-0002-4497-0194; Email: nesrin.hasirci@neu.edu.tr, nhasirci@metu.edu.tr

Authors

Dilara Goksu Tamay − *BIOMATEN, Center of Excellence in Biomaterials and Tissue Engineering, Middle East Technical University (METU), Ankara 06800, Turkey; Department of Biotechnology, Middle East Technical University (METU), Ankara 06800, Turkey*

Seyda Gokyer − *Department of Biomedical Engineering, Ankara University, Ankara 06830, Turkey*

Jürgen Schmidt − *Team Leader Electrochemistry, INNOVENT e.V. Technology Development, Jena 07745, Germany*

Pinar Yilgor Huri − *Department of Biomedical Engineering, Ankara University, Ankara 06830, Turkey;* orcid.org/0000-0002-4912-0447

Vasif Hasirci − *BIOMATEN, Center of Excellence in Biomaterials and Tissue Engineering, Middle East Technical University (METU), Ankara 06800, Turkey; Department of Medical Engineering and Biomaterials Center, Acibadem Mehmet Ali Aydinlar University, Istanbul 34684, Turkey*

Complete contact information is available at: https://pubs.acs.org/10.1021/acsami.1c16307

https://doi.org/10.1021/acsami.1c16307
ACS Appl. Mater. Interfaces 2022, 14, 104−122

Author Contributions

††A.V. and N.H. contributed equally as the corresponding authors.

Author Contributions

N.H. and A.V. designed the project and the scheme of the workload. J.S. prepared the materials. D.G.T. and V.H. carried out the cell culture experiments. S.G. and P.Y.H. carried out noncontact cytotoxicity experiments. N.H. also supervised characterization tests and prepared the manuscript. All authors contributed to bringing the data together and the discussion of the results.

Notes

The authors declare no competing financial interest.

■ ACKNOWLEDGMENTS

The study is supported by the grant of ERA.Net RUS-Plus project "CoatDegraBac" financed by The Scientific and Technological Research Council of Turkey (TUBITAK) (Project no. 9180035), Romanian National Authority for Scientific Research and Innovation, CCCDI-UEFISCDI (COFUND-ERANET-RUS-PLUS-CoatDegraBac no. 68/2018, within PNCDI III), and German Federal Ministry of Education and Research (Funding code 01DJ19004B). A.V. thanks Tomsk Polytechnic University within the framework of the Tomsk Polytechnic University-Competitiveness Enhancement Program grant as well as the Core Program, Project No. 18N/2019. The authors thank the Middle East Technical University (METU) Central Lab for SEM and EDS analyses. The authors also acknowledge the METU Center of Excellence in Biomaterials and Tissue Engineering (BIOMATEN) for the use of facilities.

■ REFERENCES

(1) Hasirci, V.; Hasirci, N. Introduction. In *Fundamentals of Biomaterials*; Springer: New York, 2018; pp 1−14.
(2) Moghaddam, N. S.; Andani, M. T.; Amerinatanzi, A.; Haberland, C.; Huff, S.; Miller, M.; Elahinia, M.; Dean, D. Metals for Bone Implants: Safety, Design, and Efficacy. *Biomanuf. Rev.* **2016**, *1*, No. 1.
(3) Kim, T.; See, C. W.; Li, X.; Zhu, D. Orthopedic Implants and Devices for Bone Fractures and Defects: Past, Present and Perspective. *Eng. Regener.* **2020**, *1*, 6−18.
(4) Li, J.; Qin, L.; Yang, K.; Ma, Z.; Wang, Y.; Cheng, L.; Zhao, D. Materials Evolution of Bone Plates for Internal Fixation of Bone Fractures: A Review. *J. Mater. Sci. Technol.* **2020**, *36*, 190−208.
(5) Poologasundarampillai, G.; Nommeots-Nomm, A. Materials for 3D Printing in Medicine: Metals, Polymers, Ceramics, Hydrogels. In *3D Printing in Medicine*; Elsevier Inc, 2017; pp 43−71.
(6) Ghazizadeh, E.; Jabbari, A. H.; Sedighi, M. In Vitro Corrosion-Fatigue Behavior of Biodegradable Mg/HA Composite in Simulated Body Fluid. *J. Magnesium Alloys* **2021**, DOI: 10.1016/j.jma.2021.03.027.
(7) Sezer, N.; Evis, Z.; Kayhan, S. M.; Tahmasebifar, A.; Koç, M. Review of Magnesium-Based Biomaterials and Their Applications. *J. Magnesium Alloys* **2018**, *6*, 23−43.
(8) Sun, Y.; Helmholz, H.; Willumeit-Römer, R. Preclinical in Vivo Research of Magnesium-Based Implants for Fracture Treatment: A Systematic Review of Animal Model Selection and Study Design. *J. Magnesium Alloys* **2021**, *9*, 351−361.
(9) Staiger, M. P.; Pietak, A. M.; Huadmai, J.; Dias, G. Magnesium and Its Alloys as Orthopedic Biomaterials: A Review. *Biomaterials* **2006**, *27*, 1728−1734.
(10) Liu, C.; Wang, Q.; Han, B.; Luan, J.; Kai, J.-J.; Liu, C.-T.; Wu, G.; Lu, J. Second Phase Effect on Corrosion of Nanostructured Mg-Zn-Ca Dual-Phase Metallic Glasses. *J. Magnesium Alloys* **2021**, DOI: 10.1016/j.jma.2021.03.016.
(11) Vormann, J. Magnesium: Nutrition and Metabolism. *Mol. Aspects Med.* **2003**, *24*, 27−37.
(12) Song, G. Control of Biodegradation of Biocompatable Magnesium Alloys. *Corros. Sci.* **2007**, *49*, 1696−1701.
(13) Barati Darband, G.; Aliofkhazraei, M.; Hamghalam, P.; Valizade, N. Plasma Electrolytic Oxidation of Magnesium and Its Alloys: Mechanism, Properties and Applications. *J. Magnesium Alloys* **2017**, *5*, 74−132.
(14) Qiao, Z.; Shi, Z.; Hort, N.; Zainal Abidin, N. I.; Atrens, A. Corrosion Behaviour of a Nominally High Purity Mg Ingot Produced by Permanent Mould Direct Chill Casting. *Corros. Sci.* **2012**, *61*, 185−207.
(15) Witte, F. The History of Biodegradable Magnesium Implants: A Review. *Acta Biomater.* **2010**, *6*, 1680−1692.
(16) Zheng, Y. F.; Gu, X. N.; Witte, F. Biodegradable Metals. *Mater. Sci. Eng., R* **2014**, *77*, 1−34.
(17) Westengen, H.; Aune, T. K.; Kammer, C. Magnesium Casting Alloys. In *Magnesium Technology: Metallurgy, Design Data, Applications*; Friedrich, H. E.; Mordike, B. L., Eds.; Springer: Berlin Heidelberg, 2006; pp 145−218.
(18) Khan, S. N.; Warkhedkar, R. M.; Shyam, A. K.. Human Bone Strength Evaluation through Different Mechanical Tests. *Int. J. Curr. Eng. Technol.* **2013**, *2*, 539−543.
(19) Xin, Y.; Huo, K.; Tao, H.; Tang, G.; Chu, P. K. Influence of Aggressive Ions on the Degradation Behavior of Biomedical Magnesium Alloy in Physiological Environment. *Acta Biomater.* **2008**, *4*, 2008−2015.
(20) Zhang, B. P.; Wang, Y.; Geng, L. Research on Mg-Zn-Ca Alloy as Degradable Biomaterial. *Biomater. - Phys. Chem.* **2011**, DOI: 10.5772/23929.
(21) Chen, J.; Tan, L.; Yu, X.; Etim, I. P.; Ibrahim, M.; Yang, K. Mechanical Properties of Magnesium Alloys for Medical Application: A Review. *J. Mech. Behav. Biomed. Mater.* **2018**, *87*, 68−79.
(22) Hoppe, A.; Güldal, N. S.; Boccaccini, A. R. A Review of the Biological Response to Ionic Dissolution Products from Bioactive Glasses and Glass-Ceramics. *Biomaterials* **2011**, *32*, 2757−2774.
(23) Yoshizawa, S.; Brown, A.; Barchowsky, A.; Sfeir, C. Magnesium Ion Stimulation of Bone Marrow Stromal Cells Enhances Osteogenic Activity, Simulating the Effect of Magnesium Alloy Degradation. *Acta Biomater.* **2014**, *10*, 2834−2842.
(24) Lee, J.-W.; Han, H.-S.; Han, K. J.; Park, J.; Jeon, H.; Ok, M. R.; Seok, H. K.; Ahn, J. P.; Lee, K. E.; Lee, D. H.; Yang, S. J.; Cho, S. Y.; Cha, P. R.; Kwon, H.; Nam, T. H.; Han, J. H.; Lo; Rho, H. J.; Lee, K. S.; Kim, Y. C.; Mantovani, D.; et al. Long-Term Clinical Study and Multiscale Analysis of in Vivo Biodegradation Mechanism of Mg Alloy. *Proc. Natl. Acad. Sci. U.S.A.* **2016**, *113*, 716−721.
(25) Pogorielov, M.; Husak, E.; Solodivnik, A.; Zhdanov, S. Magnesium-Based Biodegradable Alloys: Degradation, Application, and Alloying Elements. *Interv. Med. Appl. Sci.* **2017**, *9*, 27−38.
(26) Yang, Y.; He, C.; Dianyu, E.; Yang, W.; Qi, F.; Xie, D.; Shen, L.; Peng, S.; Shuai, C. Mg Bone Implant: Features, Developments and Perspectives. *Mater. Des.* **2020**, *185*, No. 108259.
(27) Mei, D.; Lamaka, S. V.; Gonzalez, J.; Feyerabend, F.; Willumeit-Römer, R.; Zheludkevich, M. L. The Role of Individual Components of Simulated Body Fluid on the Corrosion Behavior of Commercially Pure Mg. *Corros. Sci.* **2019**, *147*, 81−93.
(28) Zhang, Y.; Huang, Y.; Feyerabend, F.; Blawert, C.; Gan, W.; Maawad, E.; You, S.; Gavras, S.; Scharnagl, N.; Bode, J.; Vogt, C.; Zander, D.; Willumeit-Römer, R.; Kainer, K. U.; Hort, N. Influence of the Amount of Intermetallics on the Degradation of Mg-Nd Alloys under Physiological Conditions. *Acta Biomater.* **2021**, *121*, 695−712.
(29) Wu, G.; Wang, C.; Sun, M.; Ding, W. Recent Developments and Applications on High-Performance Cast Magnesium Rare-Earth Alloys. *J. Magnesium Alloys* **2021**, *9*, 1−20.
(30) Gu, X.; Zheng, Y.; Cheng, Y.; Zhong, S.; Xi, T. In Vitro Corrosion and Biocompatibility of Binary Magnesium Alloys. *Biomaterials* **2009**, *30*, 484−498.

(31) Yin, Z. Z.; Qi, W. C.; Zeng, R. C.; Chen, X. B.; Gu, C. D.; Guan, S. K.; Zheng, Y. F. Advances in Coatings on Biodegradable Magnesium Alloys. *J. Magnesium Alloys* **2020**, *8*, 42−65.
(32) Kim, W. C.; Kim, J. G.; Lee, J. Y.; Seok, H. K. Influence of Ca on the Corrosion Properties of Magnesium for Biomaterials. *Mater. Lett.* **2008**, *62*, 4146−4148.
(33) Mohamad Rodzi, S. N. H.; Zuhailawati, H.; Dhindaw, B. K. Mechanical and Degradation Behaviour of Biodegradable Magnesium−Zinc/Hydroxyapatite Composite with Different Powder Mixing Techniques. *J. Magnesium Alloys* **2019**, *7*, 566−576.
(34) Yadav, V. S.; Sankar, M. R.; Pandey, L. M. Coating of Bioactive Glass on Magnesium Alloys to Improve Its Degradation Behavior: Interfacial Aspects. *J. Magnesium Alloys* **2020**, *8*, 999−1015.
(35) Fischer, J.; Prosenc, M. H.; Wolff, M.; Hort, N.; Willumeit, R.; Feyerabend, F. Interference of Magnesium Corrosion with Tetrazolium-Based Cytotoxicity Assays. *Acta Biomater.* **2010**, *6*, 1813−1823.
(36) Chen, Y.; Zhang, S.; Li, J.; Song, Y.; Zhao, C.; Wang, H.; Zhang, X. Influence of Mg2+ Concentration, PH Value and Specimen Parameter on the Hemolytic Property of Biodegradable Magnesium. *Mater. Sci. Eng., B* **2011**, *176*, 1823−1826.
(37) Ohsawa, I.; Ishikawa, M.; Takahashi, K.; Watanabe, M.; Nishimaki, K.; Yamagata, K.; Katsura, K. I.; Katayama, Y.; Asoh, S.; Ohta, S. Hydrogen Acts as a Therapeutic Antioxidant by Selectively Reducing Cytotoxic Oxygen Radicals. *Nat. Med.* **2007**, *13*, 688−694.
(38) Ohno, K.; Ito, M.; Ichihara, M.; Ito, M. Molecular Hydrogen as an Emerging Therapeutic Medical Gas for Neurodegenerative and Other Diseases. *Oxid. Med. Cell. Longevity* **2012**, *2012*, 1−11.
(39) Schaller, B.; Saulacic, N.; Imwinkelried, T.; Beck, S.; Liu, E. W. Y.; Gralla, J.; Nakahara, K.; Hofstetter, W.; Iizuka, T. In Vivo Degradation of Magnesium Plate/Screw Osteosynthesis Implant Systems: Soft and Hard Tissue Response in a Calvarial Model in Miniature Pigs. *J. Cranio-Maxillofac. Surg.* **2016**, *44*, 309−317.
(40) Kim, Y. K.; Lee, K. B.; Kim, S. Y.; Bode, K.; Jang, Y. S.; Kwon, T. Y.; Jeon, M. H.; Lee, M. H. Gas Formation and Biological Effects of Biodegradable Magnesium in a Preclinical and Clinical Observation. *Sci. Technol. Adv. Mater.* **2018**, *19*, 324−335.
(41) Nguyen, A.; Kunert, M.; Hort, N.; Schrader, C.; Weisser, J.; Schmidt, J. Cytotoxicity of the Ga-Containing Coatings on Biodegradable Magnesium Alloys. *Surf. Innovations* **2015**, *3*, 10−19.
(42) Li, Z.; Gu, X.; Lou, S.; Zheng, Y. The Development of Binary Mg-Ca Alloys for Use as Biodegradable Materials within Bone. *Biomaterials* **2008**, *29*, 1329−1344.
(43) Wan, Y. Z.; Xiong, G. Y.; Luo, H. L.; He, F.; Huang, Y.; Wang, Y. L. Influence of Zinc Ion Implantation on Surface Nanomechanical Performance and Corrosion Resistance of Biomedical Magnesium-Calcium Alloys. *Appl. Surf. Sci.* **2008**, *254*, 5514−5516.
(44) Du, H.; Wei, Z.; Liu, X.; Zhang, E. Effects of Zn on the Microstructure, Mechanical Property and Bio-Corrosion Property of Mg-3Ca Alloys for Biomedical Application. *Mater. Chem. Phys.* **2011**, *125*, 568−575.
(45) Guo, K.; Liu, M.; Wang, J.; Sun, Y.; Li, W.; Zhu, S.; Wang, L.; Guan, S. Microstructure and Texture Evolution of Fine-Grained Mg-Zn-Y-Nd Alloy Micro-Tubes for Biodegradable Vascular Stents Processed by Hot Extrusion and Rapid Cooling. *J. Magnesium Alloys* **2020**, *8*, 873−882.
(46) Bazhenov, V.; Koltygin, A.; Komissarov, A.; Li, A.; Bautin, V.; Khasenova, R.; Anishchenko, A.; Seferyan, A.; Komissarova, J.; Estrin, Y. Gallium-Containing Magnesium Alloy for Potential Use as Temporary Implants in Osteosynthesis. *J. Magnesium Alloys* **2020**, *8*, 352−363.
(47) Kawamura, H.; Ito, A.; Miyakawa, S.; Layrolle, P.; Ojima, K.; Ichinose, N.; Tateishi, T. Stimulatory Effect of Zinc-Releasing Calcium Phosphate Implant on Bone Formation in Rabbit Femora. *J. Biomed. Mater. Res.* **2000**, *50*, 184−190.
(48) Huang, Y.; Zhang, X.; Mao, H.; Li, T.; Zhao, R.; Yan, Y.; Pang, X. Osteoblastic Cell Responses and Antibacterial Efficacy of Cu/Zn Co-Substituted Hydroxyapatite Coatings on Pure Titanium Using Electrodeposition Method. *RSC Adv.* **2015**, *5*, 17076−17086.
(49) Almoudi, M. M.; Hussein, A. S.; Abu Hassan, M. I.; Mohamad Zain, N. A Systematic Review on Antibacterial Activity of Zinc against Streptococcus Mutans. *Saudi Dent. J.* **2018**, *30*, 283−291.
(50) Predoi, D.; Iconaru, S. L.; Predoi, M. V.; Motelica-Heino, M.; Guegan, R.; Buton, N. Evaluation of Antibacterial Activity of Zinc-Doped Hydroxyapatite Colloids and Dispersion Stability Using Ultrasounds. *Nanomaterials* **2019**, *9*, 515.
(51) Stanić, V.; Dimitrijević, S.; Antić-Stanković, J.; Mitrić, M.; Jokić, B.; Plećaš, I. B.; Raičević, S. Synthesis, Characterization and Antimicrobial Activity of Copper and Zinc-Doped Hydroxyapatite Nanopowders. *Appl. Surf. Sci.* **2010**, *256*, 6083−6089.
(52) Thian, E. S.; Konishi, T.; Kawanobe, Y.; Lim, P. N.; Choong, C.; Ho, B.; Aizawa, M. Zinc-Substituted Hydroxyapatite: A Biomaterial with Enhanced Bioactivity and Antibacterial Properties. *J. Mater. Sci. Mater. Med.* **2013**, *24*, 437−445.
(53) Nguyen, A.; Kunert, M.; Hort, N.; Schrader, C.; Weisser, J.; Schmidt, J. Cytotoxicity of the Ga-Containing Coatings on Biodegradable Magnesium Alloys. *Surf. Innovations* **2015**, *3*, 10−19.
(54) Kurtjak, M.; Vukomanović, M.; Kramer, L.; Suvorov, D. Biocompatible Nano-Gallium/Hydroxyapatite Nanocomposite with Antimicrobial Activity. *J. Mater. Sci. Mater. Med.* **2016**, *27*, No. 170.
(55) Ozcan, C.; Hasirci, N. Plasma Modification of PMMA Films: Surface Free Energy and Cell-Attachment Studies. *J. Biomater. Sci., Polym. Ed.* **2007**, *18*, 759−773.
(56) Ozcan, C.; Hasirci, N. Evaluation of Surface Free Energy for PMMA Films. *J. Appl. Polym. Sci.* **2008**, *108*, 438−446.
(57) Pallas, N. R.; Pethica, B. A. The Surface Tension of Water. *Colloids Surf.* **1983**, *6*, 221−227.
(58) Kinart, C. M.; Kinart, W. J.; Kolasiński, A. The Internal Structures of Liquid N-Methylformide-N, n-Dimethylformamide Binary Mixtures. *Phys. Chem. Liq.* **1998**, *36*, 133−139.
(59) ISO 14577-1: Metallic Materials — Instrumented Indentation Test for Hardness and Materials Parameters — Part 1: Test Method, 2015.
(60) ISO 14577-1 Metallic Materials — Instrumented Indentation Test for Hardness and Materials Parameters — Part 1: Test Method, 2002.
(61) Mendes, S. C.; Reis, R. L.; Bovell, Y. P.; Cunha, A. M.; Van Blitterswijk, C. A.; De Bruijn, J. D. Biocompatibility Testing of Novel Starch-Based Materials with Potential Application in Orthopaedic Surgery: A Preliminary Study. *Biomaterials* **2001**, *22*, 2057−2064.
(62) Wu, Y.; Wang, Y.; Tian, S.; Li, H.; Zhao, Y.; Jia, D.; Zhou, Y. Formation Mechanism, Degradation Behavior, and Cytocompatibility of a Double-Layered Structural MAO/RGO-CaP Coating on AZ31 Mg. *Colloids Surf., B* **2020**, *190*, No. 110901.
(63) Lu, Y.; Wan, P.; Tan, L.; Zhang, B.; Yang, K.; Lin, J. Preliminary Study on a Bioactive Sr Containing Ca−P Coating on Pure Magnesium by a Two-Step Procedure. *Surf. Coat. Technol.* **2014**, *252*, 79−86.
(64) Lee, S. H.; Kim, H. W.; Lee, E. J.; Li, L. H.; Kim, H. E. Hydroxyapatite-TiO2 Hybrid Coating on Ti Implants. *J. Biomater. Appl.* **2006**, *20*, 195−208.
(65) Wei, D.; Zhou, Y.; Jia, D.; Wang, Y. Effect of Heat Treatment on the Structure and in Vitro Bioactivity of Microarc-Oxidized (MAO) Titania Coatings Containing Ca and P Ions. *Surf. Coat. Technol.* **2007**, *201*, 8723−8729.
(66) Vorokh, A. S. Scherrer Formula: Estimation of Error in Determining Small Nanoparticle Size. *Nanosyst.: Phys., Chem.. Math.* **2018**, 364−369.
(67) Zhao, J.; Liu, Y.; Sun, W.-b.; Yang, X. First Detection, Characterization, and Application of Amorphous Calcium Phosphate in Dentistry. *J. Dent. Sci.* **2012**, *7*, 316−323.
(68) Vranceanu, D. M.; Ionescu, I. C.; Ungureanu, E.; Cojocaru, M. O.; Vladescu, A.; Cotrut, C. M. Magnesium Doped Hydroxyapatite-Based Coatings Obtained by Pulsed Galvanostatic Electrochemical Deposition with Adjustable Electrochemical Behavior. *Coatings* **2020**, *10*, 727.
(69) Vladescu, A.; Vranceanu, D. M.; Kulesza, S.; Ivanov, A. N.; Bramowicz, M.; Fedonnikov, A. S.; Braic, M.; Norkin, I. A.; Koptyug, A.; Kurtukova, M. O.; Dinu, M.; Pana, I.; Surmeneva, M. A.; Surmenev,

R. A.; Cotrut, C. M. Influence of the Electrolyte's PH on the Properties of Electrochemically Deposited Hydroxyapatite Coating on Additively Manufactured Ti64 Alloy. *Sci. Rep.* **2017**, *7*, No. 16819.
(70) Shoar Abouzari, M. R.; Berkemeier, F.; Schmitz, G.; Wilmer, D. On the Physical Interpretation of Constant Phase Elements. *Solid State Ionics* **2009**, *180*, 922−927.
(71) Akmene, R. J.; Balodis, A. J.; Dekhtyar, Y.; Markelova, G. N.; Matvejevs, J. V.; Rozenfelds, L. B.; Sagalovich, G. L.; Smirnovs, J. S.; Tolkachovs, A. A.; Upmins, A. I. Exoelectron Emission Specrometre Complete Set of Surface Local Investigation. *Phys. Chem. Mech. Surf.* **1993**, *8*, 125−128.
(72) Kirkland, N. T.; Birbilis, N.; Staiger, M. P. Assessing the Corrosion of Biodegradable Magnesium Implants: A Critical Review of Current Methodologies and Their Limitations. *Acta Biomater.* **2012**, *8*, 925−936.
(73) Oyane, A.; Kim, H.-M.; Furuya, T.; Kokubo, T.; Miyazaki, T.; Nakamura, T. Preparation and Assessment of Revised Simulated Body Fluids. *J. Biomed. Mater. Res.* **2003**, *65A*, 188−195.
(74) Bayrak, Ö.; Asl, H. G.; Ak, A. Comparison of SBF and DMEM in Terms of Electrochemical Properties of Common Metallic Biomaterials. *Mater. Corros.* **2020**, *71*, 209−221.
(75) Popa, A. C.; Stan, G. E.; Husanu, M. A.; Mercioniu, I.; Santos, L. F.; Fernandes, H. R.; Ferreira, J. M. F. Bioglass Implant-Coating Interactions in Synthetic Physiological Fluids with Varying Degrees of Biomimicry. *Int. J. Nanomed.* **2017**, *Volume 12*, 683−707.
(76) Gonzalez, J.; Hou, R. Q.; Nidadavolu, E. P. S.; Willumeit-Römer, R.; Feyerabend, F. Magnesium Degradation under Physiological Conditions − Best Practice. *Bioact. Mater.* **2018**, *3*, 174−185.
(77) Walker, J.; Shadanbaz, S.; Kirkland, N. T.; Stace, E.; Woodfield, T.; Staiger, M. P.; Dias, G. J. Magnesium Alloys: Predicting in Vivo Corrosion with in Vitro Immersion Testing. *J. Biomed. Mater. Res., Part B* **2012**, *100B*, 1134−1141.
(78) Gao, Z.; Song, M.; Liu, R. L.; Shen, Y.; Ward, L.; Cole, I.; Chen, X. B.; Liu, X. Improving in Vitro and in Vivo Antibacterial Functionality of Mg Alloys through Micro-Alloying with Sr and Ga. *Mater. Sci. Eng., C* **2019**, *104*, No. 109926.
(79) Zhu, X.; Chen, J.; Scheideler, L.; Reichl, R.; Geis-Gerstorfer, J. Effects of Topography and Composition of Titanium Surface Oxides on Osteoblast Responses. *Biomaterials* **2004**, *25*, 4087−4103.
(80) Sedelnikova, M. B.; Komarova, E. G.; Sharkeev, Y. P.; Chebodaeva, V. V.; Tolkacheva, T. V.; Kondranova, A. M.; Zakharenko, A. M.; Bakina, O. V. Effect of the Porosity, Roughness, Wettability, and Charge of Micro-Arc Coatings on the Efficiency of Doxorubicin Delivery and Suppression of Cancer Cells. *Coatings* **2020**, *10*, 664.
(81) Kocijan, A.; Conradi, M.; Hočevar, M. The Influence of Surface Wettability and Topography on the Bioactivity of TiO2/Epoxy Coatings on AISI 316L Stainless Steel. *Materials* **2019**, *12*, 1877.
(82) Das, K.; Bose, S.; Bandyopadhyay, A. Surface Modifications and Cell-Materials Interactions with Anodized Ti. *Acta Biomater.* **2007**, *3*, 573−585.
(83) Liu, X.; Lim, J. Y.; Donahue, H. J.; Dhurjati, R.; Mastro, A. M.; Vogler, E. A. Influence of Substratum Surface Chemistry/Energy and Topography on the Human Fetal Osteoblastic Cell Line HFOB 1.19: Phenotypic and Genotypic Responses Observed in Vitro. *Biomaterials* **2007**, *28*, 4535−4550.
(84) Pegueroles, M.; Gil, F. J.; Planell, J. A.; Aparicio, C. The Influence of Blasting and Sterilization on Static and Time-Related Wettability and Surface-Energy Properties of Titanium Surfaces. *Surf. Coat. Technol.* **2008**, *202*, 3470−3479.
(85) Harnett, E. M.; Alderman, J.; Wood, T. The Surface Energy of Various Biomaterials Coated with Adhesion Molecules Used in Cell Culture. *Colloids Surf., B* **2007**, *55*, 90−97.
(86) Yang, H.; Jia, B.; Zhang, Z.; Qu, X.; Li, G.; Lin, W.; Zhu, D.; Dai, K.; Zheng, Y. Alloying Design of Biodegradable Zinc as Promising Bone Implants for Load-Bearing Applications. *Nat. Commun.* **2020**, *11*, No. 401.
(87) Gupta, M.; Meenashisundaram, G. K. Insight into Designing Biocompatible Magnesium Alloys and Composites. In *SpringerBriefs in Materials*; Springer: Singapore, 2015.
(88) Ding, Y.; Wen, C.; Hodgson, P.; Li, Y. Effects of Alloying Elements on the Corrosion Behavior and Biocompatibility of Biodegradable Magnesium Alloys: A Review. *J. Mater. Chem. B* **2014**, *2*, 1912−1933.
(89) Si, J.; Shen, H.; Miao, H.; Tian, Y.; Huang, H.; Shi, J.; Yuan, G.; Shen, G. In Vitro and in Vivo Evaluations of Mg-Zn-Gd Alloy Membrane on Guided Bone Regeneration for Rabbit Calvarial Defect. *J. Magnesium Alloys* **2021**, *9*, 281−291.
(90) Ma, Z.; Fu, Q. Therapeutic Effect of Organic Gallium on Ovariectomized Osteopenic Rats by Decreased Serum Minerals and Increased Bone Mineral Content. *Biol. Trace Elem. Res.* **2010**, *133*, 342−349.
(91) Yamamoto, A.; Hiromoto, S. Effect of Inorganic Salts, Amino Acids and Proteins on the Degradation of Pure Magnesium in Vitro. *Mater. Sci. Eng., C* **2009**, *29*, 1559−1568.
(92) Amaravathy, P.; Sowndarya, S.; Sathyanarayanan, S.; Rajendran, N. Novel Sol Gel Coating of Nb2O5 on Magnesium Alloy for Biomedical Applications. *Surf. Coat. Technol.* **2014**, *244*, 131−141.
(93) Kunjukunju, S.; Roy, A.; Ramanathan, M.; Lee, B.; Candiello, J. E.; Kumta, P. N. A Layer-by-Layer Approach to Natural Polymer-Derived Bioactive Coatings on Magnesium Alloys. *Acta Biomater.* **2013**, *9*, 8690−8703.
(94) Liu, X. L.; Zhou, W. R.; Wu, Y. H.; Cheng, Y.; Zheng, Y. F. Effect of Sterilization Process on Surface Characteristics and Biocompatibility of Pure Mg and MgCa Alloys. *Mater. Sci. Eng., C* **2013**, *33*, 4144−4154.
(95) Salahshoor, M.; Guo, Y. Biodegradable Orthopedic Magnesium-Calcium (MgCa) Alloys, Processing, and Corrosion Performance. *Materials* **2012**, *5*, 135−155.
(96) Komarova, E. G.; Sharkeev, Y. P.; Sedelnikova, M. B.; Prosolov, K. A.; Khlusov, I. A.; Prymak, O.; Epple, M. Zn- or Cu-Containing CaP-Based Coatings Formed by Micro-Arc Oxidation on Titanium and Ti-40Nb Alloy: Part I-Microstructure, Composition and Properties. *Materials* **2020**, *13*, 4116.
(97) Abbasi, S.; Aliofkhazraei, M.; Mojiri, H.; Amini, M.; Ahmadzadeh, M.; Shourgeshty, M. Corrosion Behavior of Pure Mg and AZ31 Magnesium Alloy. *Prot. Met. Phys. Chem. Surf.* **2017**, *53*, 573−578.
(98) Witte, F.; Fischer, J.; Nellesen, J.; Crostack, H.-A.; Kaese, V.; Pisch, A.; Beckmann, F.; Windhagen, H. In Vitro and in Vivo Corrosion Measurements of Magnesium Alloys. *Biomaterials* **2006**, *27*, 1013−1018.
(99) Pan, Y. K.; Chen, C. Z.; Wang, D. G.; Yu, X. Microstructure and Biological Properties of Micro-Arc Oxidation Coatings on ZK60 Magnesium Alloy. *J. Biomed. Mater. Res., Part B* **2012**, *100B*, 1574−1586.
(100) Liu, G. Y.; Hu, J.; Ding, Z. K.; Wang, C. Bioactive Calcium Phosphate Coating Formed on Micro-Arc Oxidized Magnesium by Chemical Deposition. *Appl. Surf. Sci.* **2011**, *257*, 2051−2057.
(101) Cipriano, A. F.; Zhao, T.; Johnson, I.; Guan, R. G.; Garcia, S.; Liu, H. In Vitro Degradation of Four Magnesium-Zinc-Strontium Alloys and Their Cytocompatibility with Human Embryonic Stem Cells. *J. Mater. Sci. Mater. Med.* **2013**, *24*, 989−1003.

https://doi.org/10.1021/acsami.1c16307
ACS Appl. Mater. Interfaces 2022, 14, 104−122